

University of Nebraska - Lincoln

DigitalCommons@University of Nebraska - Lincoln

Mechanical (and Materials) Engineering --
Dissertations, Theses, and Student Research

Mechanical & Materials Engineering,
Department of

Spring 4-17-2020

Thermal Modeling of Additive Manufacturing Using Graph Theory: Validation with Directed Energy Deposition

Jordan Severson

University of Nebraska - Lincoln, jordanseverson14@gmail.com

Follow this and additional works at: <https://digitalcommons.unl.edu/mechengdiss>



Part of the [Heat Transfer, Combustion Commons](#), [Manufacturing Commons](#), [Materials Science and Engineering Commons](#), and the [Structures and Materials Commons](#)

Severson, Jordan, "Thermal Modeling of Additive Manufacturing Using Graph Theory: Validation with Directed Energy Deposition" (2020). *Mechanical (and Materials) Engineering -- Dissertations, Theses, and Student Research*. 152.

<https://digitalcommons.unl.edu/mechengdiss/152>

This Article is brought to you for free and open access by the Mechanical & Materials Engineering, Department of at DigitalCommons@University of Nebraska - Lincoln. It has been accepted for inclusion in Mechanical (and Materials) Engineering -- Dissertations, Theses, and Student Research by an authorized administrator of DigitalCommons@University of Nebraska - Lincoln.

THERMAL MODELING OF ADDITIVE MANUFACTURING USING
GRAPH THEORY: VALIDATION WITH DIRECTED ENERGY
DEPOSITION

by

Jordan A. Severson

A THESIS

Presented to the Faculty of

The Graduate College at the University of Nebraska

In Partial Fulfillment of Requirements

For the Degree of Master of Science

Major: Mechanical Engineering and Applied Mechanics

Under the Supervision of Professors Prahalada Rao and Kevin Cole

Lincoln, Nebraska

May 2020

THERMAL MODELING OF ADDITIVE MANUFACTURING USING GRAPH THEORY: VALIDATION WITH DIRECTED ENERGY DEPOSITION

Jordan Alan Severson, M.S.
University of Nebraska, 2020

Advisors: Prahalada K. Rao and Kevin D. Cole

Metal additive manufacturing (AM/3D printing) offers unparalleled advantages over conventional manufacturing, including greater design freedom and a lower lead time. However, the use of AM parts in safety-critical industries, such as aerospace and biomedical, is limited by the tendency of the process to create flaws that can lead to sudden failure during use. The root cause of flaw formation in metal AM parts, such as porosity and deformation, is linked to the temperature inside the part during the process, called the thermal history. The thermal history is a function of the process parameters and part design.

Consequently, the first step towards ensuring consistent part quality in metal AM is to understand how and why the process parameters and part geometry influence the thermal history. Given the current lack of scientific insight into the causal design-process-thermal physics link that governs part quality, AM practitioners resort to expensive and time-consuming trial-and-error tests to optimize part geometry and process parameters.

An approach to reduce extensive empirical testing is to identify the viable process parameters and part geometry combinations through rapid thermal simulations. However,

a major barrier that deters physics-based design and process optimization efforts in AM is the prohibitive computational burden of existing finite element-based thermal modeling.

The *objective* of this thesis is to understand the causal effect of process parameters on the temperature distribution in AM parts using the theory of heat dissipation on graphs (graph theory). We develop and apply a novel graph theory-based computational thermal modeling approach for predicting the thermal history of titanium alloy parts made using the directed energy deposition metal AM process. As an example of the results obtained for one of the three test parts studied in this work, the temperature trends predicted by the graph theory approach had error ~11% compared to experimental trends. Moreover, the graph theory simulation was obtained within 9 minutes, which is less than the 25 minutes required to print the part.

Table of Contents

Acknowledgements.....	5
1 Introduction	6
1.1 Background.....	6
1.2 Goal and Motivation	10
2 Literature	12
2.1 Simulation.....	12
2.2 Computation Techniques	14
2.3 Validation.....	15
3 Methods.....	17
3.1 Experiments	17
3.1.1 Temperature Measurements	21
3.2 Simulation Procedure.....	22
3.2.1 Implementation.....	28
3.2.2 Sensor Location	31
3.2.3 Neighborhood size.....	32
3.2.4 Weight Scaling	34
3.2.5 Transient Material Properties	35

	2
3.3 Goldak's Double Ellipsoid Heat Source Model.....	36
4 Results	43
4.1 Case A Results	43
4.2 Case B Results	47
4.3 Case C Results	51
5 Conclusions and Future Work.....	55
Appendix A. Heat Transfer Coefficient Calculation	63
References Cited.....	64

List of Figures

Figure 1. (a) LPBF process schematic and (b) DED process schematic. In DED, metal powder is sprayed via nozzles and fused onto a substrate by a laser beam.	7
Figure 2. Lack-of-fusion defects in a titanium part made with LPBF. These same defects are common in DED.	7
Figure 3. Salient thermal phenomena in DED include conductive, convective, and radiative heat transfer.	8
Figure 4. Experimental data for each deposition case along with the corresponding thermocouple location and dwell time.	19
Figure 5. A schematic of (a) the clamped substrate in relation to the thin wall, (b) Case A and B, and (c) Case C.	20
Figure 6. Thermocouple locations for each case.	21
Figure 7. Representation of the four steps in the graph-theoretic approach for the DED process.	23
Figure 8. Block-by-block heating scheme used in graph theory DED simulation. ...	25
Figure 9. Heat transfer with neighborhood number vs. neighborhood size.	33
Figure 10. The effect of the scaling factor C on the melt pool temperature, as a function of (a) the melt pool length, and (b) the melt pool depth.	39
Figure 11. (a) Top View and (b) Side View of melt pool.	41
Figure 12. Snapshots of the graph theory-based simulation for each case. The lack of dwell time in Case B and Case C leads to accumulation of heat in the top layers of the part.	44

Figure 13. Simulation results for Case A.....	46
Figure 14. Simulation results for Case B.....	50
Figure 15. Simulation results for Case C.....	53
Figure 16. Case-wise comparison between the experiment, graph-theoretic model, and Heigel, et al. model.....	55
Figure 17. Case-wise radiation loss effects at melt pool temperature of 2200 °C and lowest node density.....	61

Acknowledgements

I would like to thank my family for their unwavering support. Thank you for letting me vent and always offering valuable wisdom. Thank you, Anna, for always being understanding and a great listener. I especially want to thank my parents, who have always set a good example for me and helped me every step of the way.

Finally, I want to thank my research advisors for their guidance and patience throughout my graduate school career. I have learned many lessons relating to engineering but also ones that are best applied in everyday life. I appreciate you always encouraging me to push the bounds and explore something new.

I thank Dr. Jarred Heigel for sharing the temperature data for the three thin wall builds reported in this work.

This work is funded by the National Science Foundation grant CMMI 1752069.

1 Introduction

1.1 Background

Metal additive manufacturing (AM) processes, such as laser powder bed fusion (LPBF) and directed energy deposition (DED), offer considerable advantages over other conventional manufacturing methods. While noteworthy differences between the two AM processes are discussed later, schematics of LPBF and DED are presented in Figure 1. Compared to conventional subtractive processes, AM often requires lower lead times and allows for greater design freedom. However, inconsistencies in the process and part quality currently prevent AM from being widely accepted in critical applications. The part is often pervaded by heterogeneous microstructures and defects, such as pores and cracks. Process parameters can directly lead to the formation of certain defects. For instance, Figure 2 depicts one type of defect that is caused by a phenomenon known as lack of fusion (LOF). Although the defects in Figure 2 are taken from an LPBF part, LOF also appears in DED. As the name suggests, it occurs when the laser power is too low or the scan speed is too high, which results in incomplete melting of the metal powder particles. The part is then left with irregular voids, thus giving rise to potentially catastrophic stress concentrations.

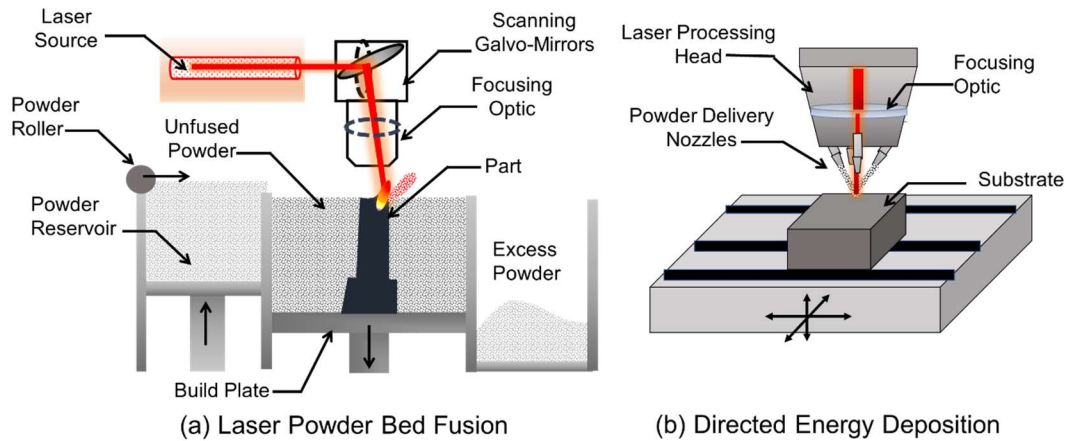


Figure 1. (a) LPBF process schematic and (b) DED process schematic. In DED, metal powder is sprayed via nozzles and fused onto a substrate by a laser beam.

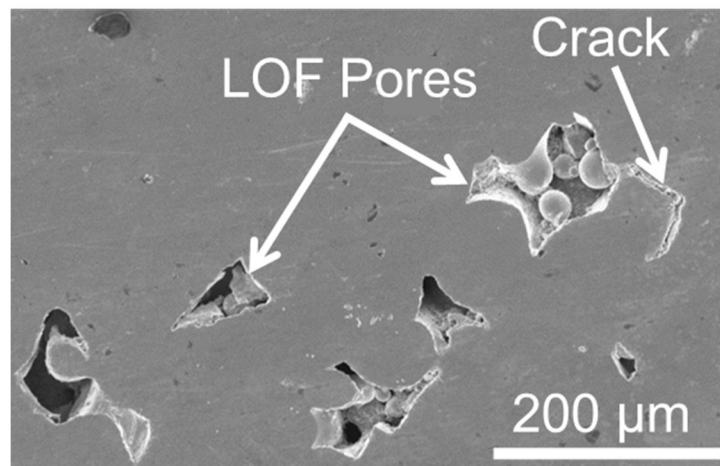


Figure 2. Lack-of-fusion defects in a titanium part made with LPBF. These same defects are common in DED.

Previous works have already proven graph theory to be a powerful tool in the thermal modeling of LPBF [1-4]. In contrast, this work focuses on DED, which poses a greater challenge for any thermal model. There are currently very few thermal models that can provide an accurate and repeatable prediction for any given material and geometry in the DED process. The proposed graph-theoretic model, a mesh-free approach, could fill a large

need for a dependable thermal model that can provide a predicted temperature distribution in a matter of minutes on a desktop computer.

Figure 3 outlines the salient thermal phenomena in DED [5]. In Figure 3, the phenomena labeled 3, 4, and 5 are unique to DED and are not present in the LPBF process. Consequently, certain heat transfer-related assumptions made in the context of the LPBF process to aid computation in our previous work must be relaxed for the DED process [1].

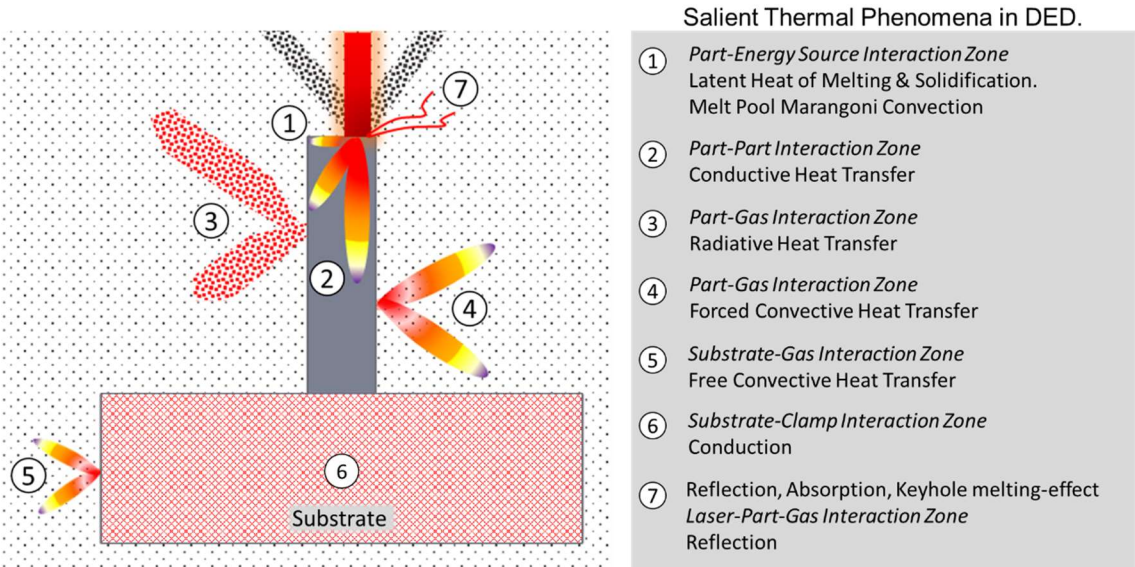


Figure 3. Salient thermal phenomena in DED include conductive, convective, and radiative heat transfer.

The first and most important difference between LPBF and DED is that in the former process, the part is surrounded by unfused powder material, viz., an insulating medium. Hence, heat loss on the top surface of the part occurs through radiation and forced convective heat transfer from the melt pool. Heat loss in the rest of the LPBF part occurs largely through conduction, albeit, heat loss through free convection occurs at the part-powder boundaries given air gaps in the unfused metal powder surrounding the part.

In contrast, as shown in Figure 3, the part in DED is surrounded not by metal powder but by an inert gas, and therefore heat is lost to the surroundings through convection and radiation from all surfaces. Convection involves both free and forced convection, as the metal powder is delivered to the substrate via an inert carrier gas, such as argon. Consequently, for a comprehensive model of part-level thermal history in DED, it is necessary to account for heat loss through conduction, both free and forced convection, and radiation.

Second, the laser heat source-related assumptions in LPBF do not carry over to the DED process because the scan velocity and spot size (beam diameter) of the laser, and layer thickness are considerably different. In LPBF, the laser is moved by a set of mirrors and the mirrors are moved by galvanometers. By contrast, in DED, the laser head is translated by the physical motion of computer numerical controls (CNC), or in other words, CNC-based axes. Consequently, the scan velocity of the laser in DED is ten times slower compared to LPBF – the scan speed of the laser in LPBF is typically 200 to $500 \text{ mm}\cdot\text{s}^{-1}$; in DED, the scan speed is on the order of $10 \text{ mm}\cdot\text{s}^{-1}$. Further, the typical layer thickness is around $50 \text{ }\mu\text{m}$ in LPBF, compared to $\sim 100 \text{ }\mu\text{m}$ to $200 \text{ }\mu\text{m}$ for DED. Lastly, the laser beam diameter in the DED process is typically nearer to the millimeter range compared to $\sim 50 \text{ }\mu\text{m}$ to $100 \text{ }\mu\text{m}$ in LPBF.

From a thermal modeling perspective, the higher laser scan velocity and smaller layer thickness of LPBF are advantageous for reducing the computation time. Researchers often simulate the deposition of multiple layers at a time in LPBF (called the super-layer or meta-layer assumption) to reduce the computation time [6]. For example, Williams, et al. use

the meta-layer assumption in an FE-model to predict thermal-induced deformation in LPBF. Meta-layers ranging from 12 to as large as 50 times the actual layer thickness (50 μm) are simulated. Williams, et al. show that their model predicts distortion within 5% of measurements, despite simulating the deposition of ~ 15 layers at a time. The slow scan speed and large laser spot size of DED ensure that the melt pool has a large diameter and penetrates deeper into the previous layers compared to LPBF. Consequently, the meta-layer assumption is not viable in DED.

1.2 Goal and Motivation

The goal of this work is to validate the graph theory approach for thermal modeling for AM in the context of the DED process. In the DED process, material in the form of powder is melted on account of energy supplied by a laser. Metal powder material in aerosolized form is delivered onto the substrate via nozzles and injected into the path of a high-power laser. The thermal phenomena at the melt pool scale, coupled with the part-level temperature distribution, influence the formation of defects and govern the microstructural evolution. These thermal aspects in turn are linked to the process parameters and design of the part. Consequently, the first step towards ensuring consistent part quality in DED is to understand the fundamental link between the process parameters, thermal phenomena, and part properties.

The graph theory approach for thermal modeling in AM has been published in the context of the LPBF process [1-4]. Theoretical verification with finite element (FE) modeling shows that the graph theory approach predicts the temperature distribution in LPBF parts within about $1/10^{\text{th}}$ of the time required by commercial FE solutions and with

errors fewer than 10%. The approach has also been validated with experimental data from the LPBF process. The author now takes this work forward by validating the approach in terms of the DED experiment run by Heigel, et al. [7, 8].

2 Literature

2.1 Simulation

Determination of an AM part's thermal history is crucial to its functional integrity [5, 9]. Various approaches have been taken by researchers to model the DED process. The majority have attempted to simulate the process with finite element analysis (FEA) by transferring the same principles that apply in weld modeling [10-19]. For certain process phenomena, weld modeling principles are transferrable. For instance, the double ellipsoid model proposed by Goldak is commonly used to approximate the melt pool shape and temperature in DED [7, 8]. Goldak's model was originally developed for welding [20]. A version of the double ellipsoid model is used in this work to describe the laser heat source.

Conversely, a major difference between DED and welding relates to the volume of the deposited material. In the welding process, the newly deposited material often composes a small fraction of the overall part since welding often only occurs along seams and junctions. As a result, most of the heat from the weld pool is quickly conducted away. However, in the DED process, the deposited material composes most, if not all, of the final part. This means that the entire part remains at a much higher temperature than those seen in welding since it was only recently deposited and solidified. Not only are temperatures in DED much higher as a result of the increased amount of newly deposited material, that material is also exposed to those higher temperatures for a much longer period of time. The combination of higher temperatures and longer exposure makes convective heat loss much more prevalent in DED than it does in welding processes. Therefore, a new consideration for convection must be developed for the DED process.

Numerous approaches to a new approximation for convection loss in DED have been studied. Attempting to apply an assumption common in weld modeling, some researchers have considered convective heat loss to be negligible in DED [21-24]. Others have implemented convection into their DED models by assuming it to be uniformly distributed over all surfaces. In those cases, they considered the heat loss to be equal to free convection loss in air [10, 12, 25-31]. Furthermore, some researchers have considered the forced nature of the shield gas in the process by employing a higher convection that is uniformly applied to all free surfaces [32, 33]. Still others have taken it a step further by using tools such as empirical equations or computational fluid dynamics to develop a more complex convection model [11, 34]. Finally, an effort to develop a measurement-based, forced convection model was proposed and tested by Heigel, et al. [7, 8]. Gouge, et al. detailed a comprehensive comparison between their convection model and other assumed convection regimes [35]. From their findings, they argue that a forced convection model will produce more accurate simulation results than a model that considers only free convection or no convection at all.

In this current work, a combination of free and forced convection regimes is considered and applied to the part surfaces. The convection coefficients are compared to those used by Heigel, et al. for different flow regimes in Table 1. The values used in the graph-theoretic approach are discussed in more detail later in the paper. Other notable assumptions used by Heigel, et al. were as follows: they assumed thermal symmetry, thus modeling only the half-symmetry of the part, and they included the clamp in their model. In contrast, the graph-theoretic model included the entire 3-D part geometry but not the

clamp. Nevertheless, an approximation for heat loss to the clamp was applied in the graph-theoretic approach and will be described in more detail later in the paper.

Table 1. Heat transfer coefficients used to approximate convective heat loss from part surfaces.

Heat Transfer Coefficient	Graph Theory (this work) [W·m ⁻² ·K ⁻¹]	Heigel's Model [7] [W·m ⁻² ·K ⁻¹]
Free	5.3	10
Forced	49.1	25-60

2.2 Computation Techniques

As previously mentioned, finite element modeling for welding processes forms the foundation on which DED modeling has been built. A review of FE modeling for welding is available in references [17-19, 36-39]. It is common for some parts produced by DED to have in excess of 1000 layers, which far exceeds the scope of traditional weld modeling. Considering the sheer size and complexity of many of the parts produced by DED though, it becomes evident that the modeling of this process introduces a significant computational load. Consequently, there exists a considerable need for an accurate and fast computational approach to determine a part's thermal history [40-45]. In search of a computationally efficient model, a variety of commercial software have been used to simulate the deposition process [12, 31, 46-50]. A novel technique that was specifically developed for the simulation of additive manufacturing processes was introduced by Panagiotis Michaleris [51]. In an effort to increase computational efficiency, Michaleris proposed and tested two material deposition methods: (1) the use of *quiet* and (2) *inactive* elements [52, 53]. The quiet approach assigns material properties to elements that have not yet been deposited such that they do not affect the overall analysis. In contrast, the inactive approach does not

even include elements in the analysis until they have been deposited, at which point they are activated. Although the underlying mathematical theory is different, the novel technique (graph theory) employed in this work uses a similar inactive element method.

Results from our previous work, which employed the graph-theoretic approach, showed that it was about ten times faster than the benchmark Goldak model used in conjunction with Abaqus, an FE method [1-4]. In addition, the mean absolute percentage error of the graph-theoretic approach was less than 10%, relative to the FE analysis.

2.3 Validation

It is necessary to validate any thermal model in order to assess its prediction accuracy and capabilities. The best way to validate is through experimentation. This current work used data from other literature for validation of the graph-theoretic approach [7, 8]. The experimental data used in this work was acquired via thermocouples, which are contact sensors that are well established for the purpose of in-situ temperature monitoring. Yan, et al. reviewed different part-level thermal measurement approaches for AM in a recent paper [54]. That review paper also includes a summary of numerical models for AM and corresponding validation efforts by various researchers. Among the validation efforts are many that use contactless measurement techniques, which are the most common for determining melt pool temperatures.

Despite considerable advances in in-situ monitoring techniques for AM, some inconsistencies remain regarding melt pool behavior and temperature distribution. A summary of observed, as well as predicted melt pool temperatures found by different researchers is presented in Table 2 for DED of Ti-6Al-4V. The three different melt pool

temperatures considered in this work: 1900 °C, 2200 °C, and 2450 °C, were chosen to represent the range of values observed and measured in the literature.

Table 2. Summary of melt pool temperatures found by other researchers.

Geometry	Laser Power [W]	Scan Speed [mm·s ⁻¹]	Method	Melt Pool Temperature [°C]	Publications
Thin Wall	425	8.5	Inactive Element Technique	1800 - 2000	[51]
Thin Wall	300	12.7	Pyrometer	~1850	[55]
Thin Wall	290	12.7	Pyrometer	1900-2000	[56]
Rectangular Thin Wall	300	2.0	Quiet Element Technique	2447	[57]
Cube	800	10.0	In-house Code (GAMMA)	2500	[58]
L-shaped Thin Wall	450	10.6	IR Camera	2485 ± 161	[59]
Cylinders	350	16.9	Pyrometer	2100 – 2500	[60]

3 Methods

3.1 Experiments

The experimental data for this work, shown in Figure 4, was acquired from Heigel, et al. [7, 8]. In their experiments, three so-called single-track thin walls were deposited with an Optomec® LENS MR-7 system. In a single-track thin wall, material in a layer was deposited in a single pass (i.e., a layer has only one hatch). The part material used was Ti-6Al-4V powder, which was delivered to the melt pool by a stream of inert argon gas. The gas passed through four nozzles that were positioned concentrically around the fiber laser's beam. These nozzles directed the argon gas and titanium powder mixture into the melt pool, where the argon gas shielded the melt pool while new powder particles entered the laser beam and were melted into a rapidly solidifying layer. The laser used in the process was a 500 W IPG Photonics fiber laser with a diameter of 1.5 mm. As this cyclic process was repeated, the single-track thin walls were manufactured layer by layer. The walls were deposited onto their own Ti-6Al-4V substrate with dimensions 76.2 mm × 25.4 mm × 6.4 mm (L×W×H). Each substrate was clamped at one end, as depicted in Figure 5(a). Table 3 summarizes the process conditions for each case. The distinguishing characteristics of the three deposition cases, labeled A through C, are outlined below and shown in Figure 5.

- A. A single-track wall including 62 layers with a programmed 20-second dwell time between each subsequent layer, also called the inter-layer cooling time. Deposition direction alternated for each layer. In other words, the laser traveled in one direction for odd-numbered layers and the opposite direction for even-numbered layers. The 20-second dwell refers to the added pause after the laser had reached the start

position, before deposition of the next layer. The addition of dwell time between each of the 62 layers resulted in a substantially longer production time of 20 minutes to the no-dwell Case B described below. Because of the dwell between layers there was a longer time for the heat to dissipate into the substrate before new material at higher temperature was deposited.

- B. A single-track wall including 62 layers deposited without any programmed dwell time. The author notes that there was an inherent pause of 3 seconds between the end of one layer and the beginning of the next as the deposition head repositioned and resumed powder flow. It was assumed that the inherent dwell time in between layers was 3 seconds.
- C. A single-track wall including 62 layers without any programmed dwell time. As in Case B, the inherent dwell time of 3 seconds is considered. This wall was deposited on top of the pre-existing wall described as Case B. To explain further, the thin wall in Case B was allowed to cool down to ambient temperature before deposition of the additional wall layers was initiated. The result was a single-track wall that was essentially twice the height of the Case A and Case B walls and consisted of 124 deposition layers in total.

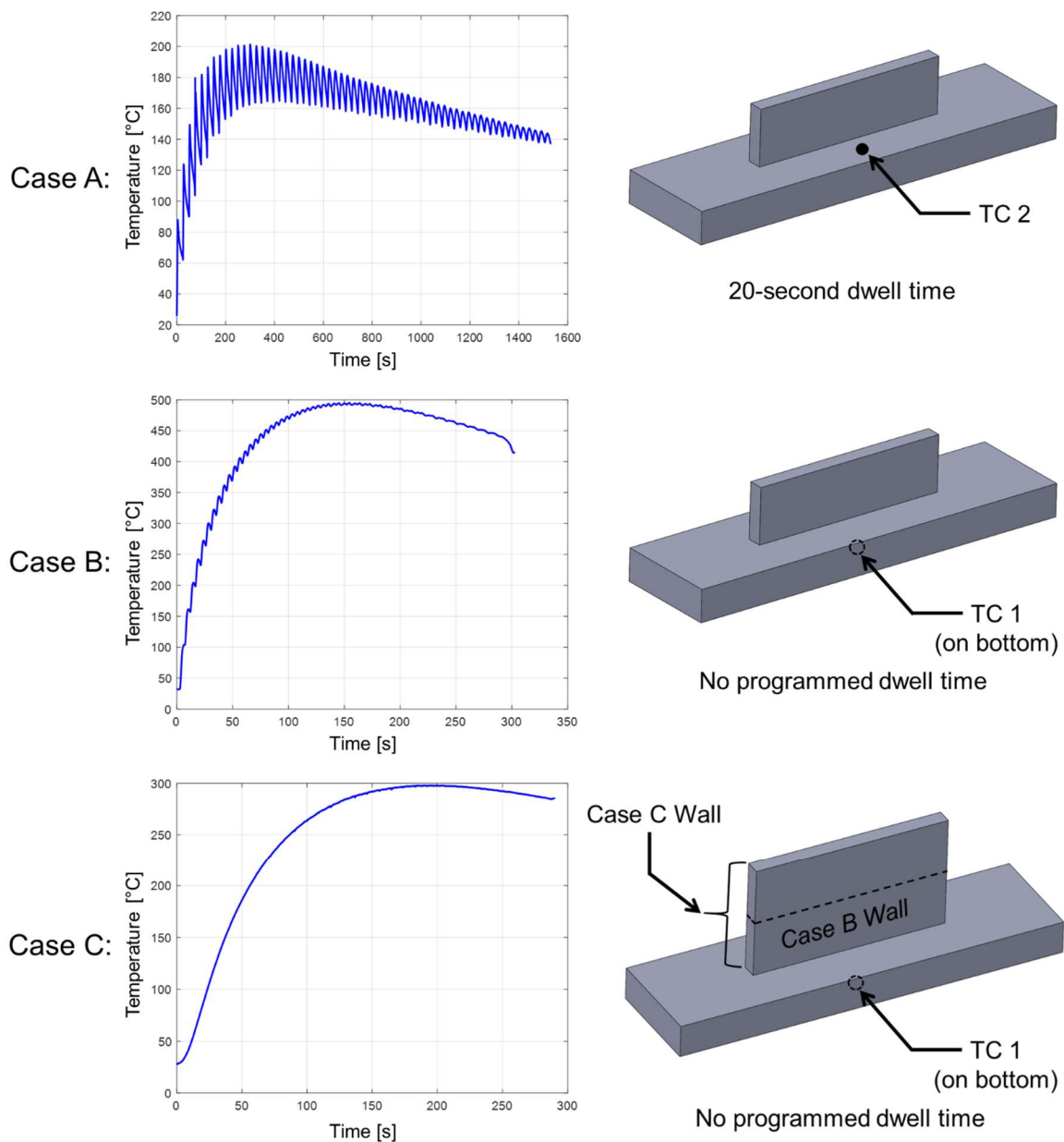


Figure 4. Experimental data for each deposition case along with the corresponding thermocouple location and dwell time.

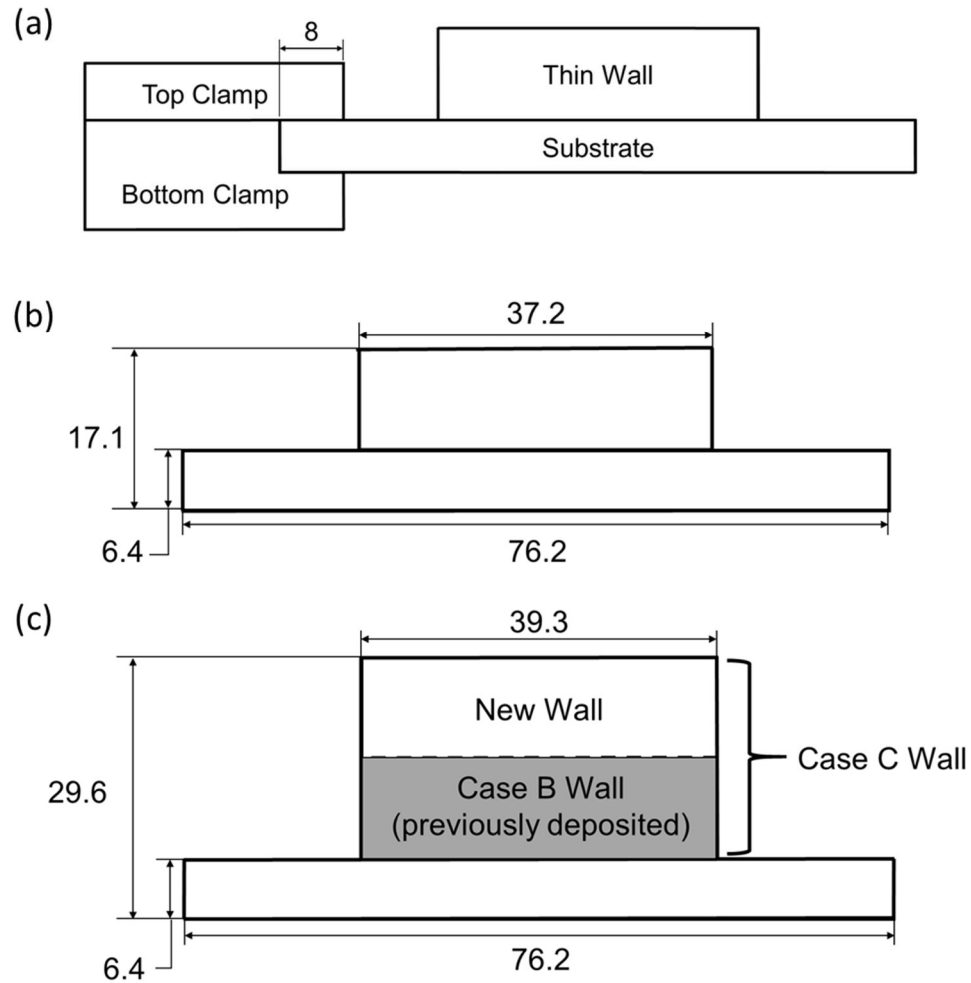


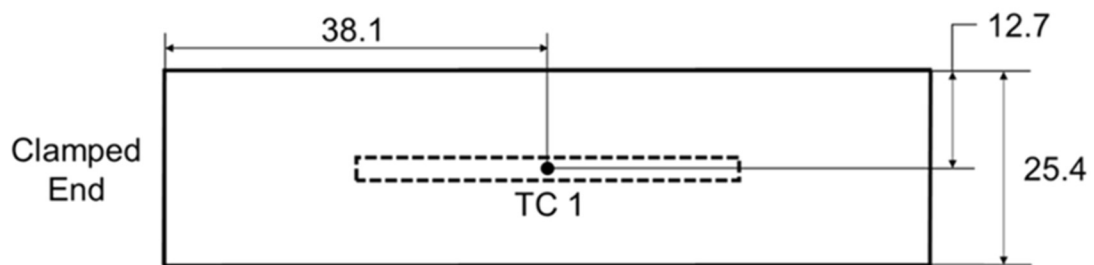
Figure 5. A schematic of (a) the clamped substrate in relation to the thin wall, (b) Case A and B, and (c) Case C.

Table 3. Process conditions for each case, detailed by Heigel et al. [7, 8].

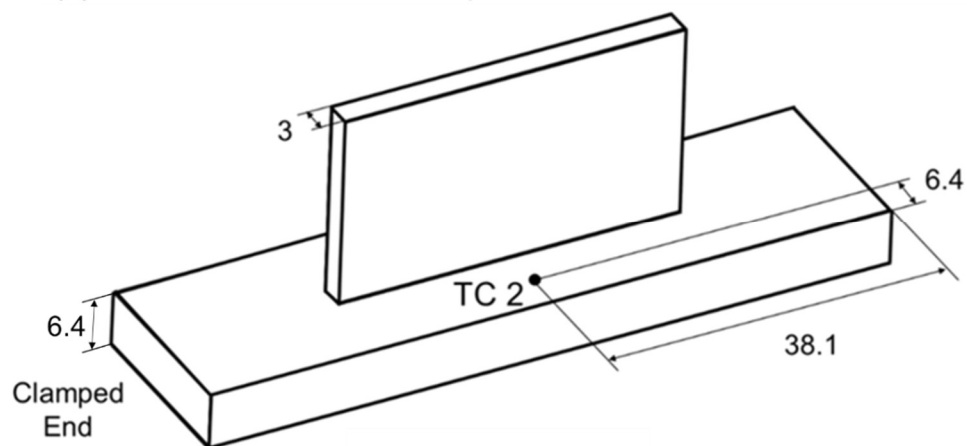
Case	A	B	C
Measured Laser Power [W]	415	410	415
Travel Speed [$\text{mm}\cdot\text{s}^{-1}$]	8.5		
Powder delivery rate [$\text{g}\cdot\text{min}^{-1}$]	3.0		
Additional dwell time [s]	20	0	0
Wall height [mm]	10.7	11.2	23.2
Measured wall length [mm]	37.2	39.2	39.3
Measured wall width [mm]	2.2	3.0	3.1
Measured Layer thickness [mm]	0.1726	0.1806	0.1871
Laser spot size [mm]	1.5		
Standoff Distance [mm]	11.4		

3.1.1 Temperature Measurements

Temperature measurements were acquired using Omega GG-K-30 type K thermocouples. Thermocouple (TC) 1 was located at the center of the substrate's bottom surface. Thermocouple 2 was located beside the thin wall's base, on the top surface of the substrate. These thermocouples were not bolted onto the substrate but appear to be brazed or spot welded to the substrate. As stated by Heigel, et al., an aluminum foil tape was used to shield the top thermocouple (TC 2) from forced convection effects during deposition of Cases A and C. However, the tape was not used during Case B, and hence temperature measurements from TC 2 were not used. Thermocouple positions are depicted in Figure 6.



(a) Bottom View: Thermocouple location for Case B and Case C



(b) Thermocouple location for Case A

Figure 6. Thermocouple locations for each case.

3.2 Simulation Procedure

The graph theory approach is distilled into four major steps. These steps are described below and pictorially represented in Figure 7. The mathematics behind each step are described in more detail in previous works [1-4].

Step 1: Discretizing the part geometry into nodes and blocks

The volume of the part to be simulated is randomly populated with nodes; the number of nodes is set at a certain number per unit volume (called node density). This discretization results in each node having a unique Cartesian (x, y, z) coordinate, i.e., the location of each node is spatially defined within the part. Next, each layer is divided into a hatch (in the case of a thin wall, each layer has only one hatch), and each hatch is further divided into discrete blocks (volumes) with a fixed height and length, with breadth equal to the hatch width.

For this study, the single track or hatch that composes each deposited layer will be broken up into five equal blocks. These discrete blocks are 7.84 mm long, 3 mm wide, and 0.1806 mm thick. There are a total of 2830 blocks in the part. The reason for dividing a hatch into blocks is explained in the context of Step 3 (Figure 8). Since the nodes are populated in a random manner, there is a degree of uncertainty in the model predictions. We quantify this uncertainty by repeating the simulations three times for each case.

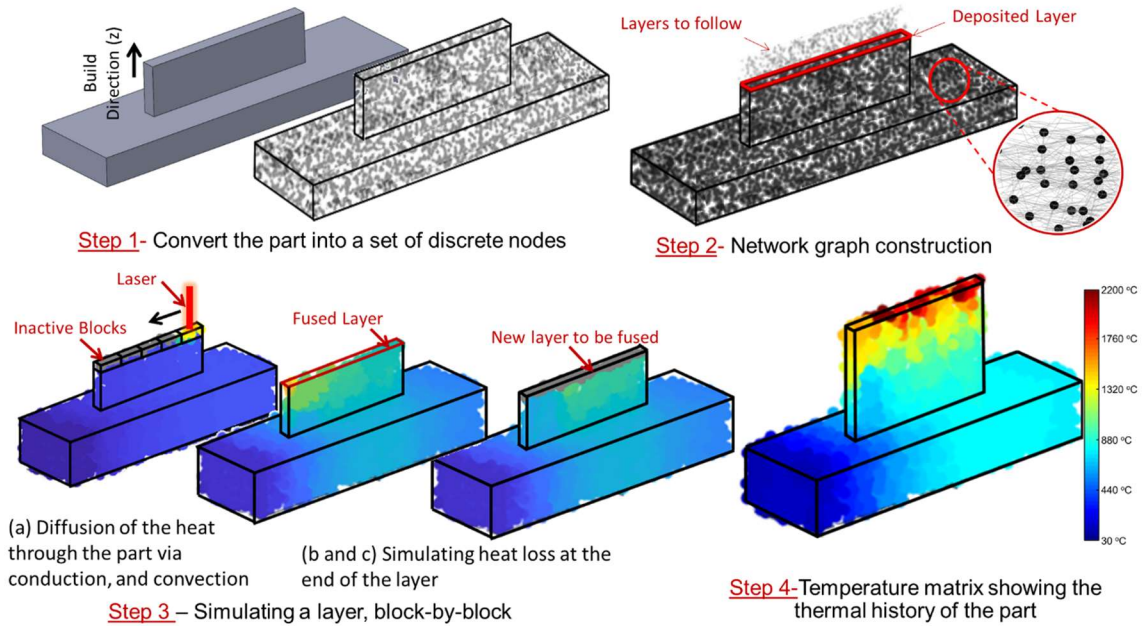


Figure 7. Representation of the four steps in the graph-theoretic approach for the DED process.

Step 2: Constructing a network graph from the cloud of discrete nodes created in Step 1

Each node is connected to its nearest neighboring nodes within a ϵ -radius. Consider ϵ [mm] as describing the radius of a sphere around a node at the center of the sphere. Nodes that fall within the volume of the sphere are connected to the node at the center of the sphere. Nodes that are outside of the sphere are not connected. This step is completed throughout the entire cloud of nodes, which results in a complex web of connections called a network graph.

Consider two nodes, π_i and π_j , whose spatial Cartesian coordinates are $c_i \equiv (x_i, y_i, z_i)$ and $c_j \equiv (x_j, y_j, z_j)$, respectively; π_i and π_j are connected by an edge having weight a_{ij} if the distance between them is less than ϵ ,

$$a_{ij} = \begin{cases} e^{-(c_i - c_j)^2 / \sigma^2} & \text{if } (c_i - c_j)^2 \leq \varepsilon \\ 0 & \text{otherwise} \end{cases} \quad (1)$$

In Eqn. (1), σ is the standard deviation of all the pairwise distances between nodes, and the exponential term is the Gaussian function that scales the distance between the nodes in the part between 0 and 1. Nodes that are farther away from each other have an edge with a smaller weight connecting each other; nodes closer to each other are connected with an edge with a larger weight,

$$\begin{aligned} \lim_{(c_i - c_j) \rightarrow 0} a_{ij} &= 1 \\ \lim_{(c_i - c_j) \rightarrow \varepsilon} a_{ij} &= 0 \end{aligned} \quad (2)$$

The neighborhood distance ε is a heuristic tunable parameter in the graph theory model, that needs to be calibrated (only once) for a material type. The calibration procedure for ε is described in Section 3.2.1.

The matrix formed by placing a_{ij} in a row i and column j is called the adjacency matrix, $\mathbf{A} = [a_{ij}]$, which is a positive symmetric matrix. From the adjacency matrix, the degree h_i of a node π_i is calculated by summing the corresponding i^{th} row (or column) of \mathbf{A} , $h_i = \sum_{\forall j} a_{ij}$. The graph Laplacian at node π_i is defined as: $l_{ij} \stackrel{\text{def}}{=} h_i - a_{ij}$, and the Laplacian matrix is obtained $\mathbf{L} = [l_{ij}]$. Finally, the eigenspectra of the graph Laplacian matrix (\mathbf{L}) will be computed as $\mathbf{L}\boldsymbol{\phi} = \boldsymbol{\Lambda}\boldsymbol{\phi}$, where $\boldsymbol{\phi}$ are the eigenvectors and $\boldsymbol{\Lambda}$ are the eigenvalues of \mathbf{L} [61].

Step 3: Block-by-block simulation of a layer

The DED simulation proceeds by heating the nodes in a block, before proceeding to the nodes in the next block. In other words, a time step involves heating of nodes inside a

block, one block at a time. Figure 8 demonstrates the block-by-block heating scheme used in this work. Since the laser scan velocity is $8.5 \text{ mm}\cdot\text{s}^{-1}$ and the length of each block is 7.84 mm long, the time to step between blocks is 0.922 s.

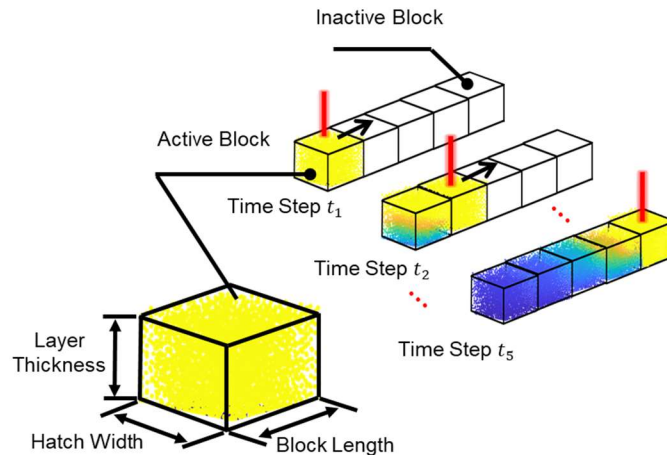


Figure 8. Block-by-block heating scheme used in graph theory DED simulation.

Step 3(a): Heat loss through conduction

After a block is heated by the laser, the heat is allowed to diffuse through the network graph that was constructed in Step 2. Conduction is the sole mode of heat transfer between the nodes. The only nodes active during this step are the ones located within layers and blocks that have already been deposited. Other nodes that are in subsequent blocks and layers remain inactive and therefore unable to transfer heat. After the heat diffuses from the block that had just been heated by the laser, the deposition of the next block is simulated. This process is repeated for every block and every layer in the part. The mathematical implications of the approach will be summarized here by only including the final derived equation, shown in Eqn. (3).

After time step t_b ($= 0.922$ s), viz, the time required to process each block, the temperature of each active node is contained in the temperature matrix \mathbf{T}_b . The temperature following heat transfer by conduction (\mathbf{T}_c) is defined as a function of the Laplacian eigenvectors (Φ) and eigenvalues (Λ) of the network graph over active nodes, where T_0 is the melt pool temperature, and g is a tunable parameter called the gain factor (g). The gain factor (g) scales the rate of thermal diffusivity or heat flux between nodes. A higher gain factor increases the rate of thermal diffusion through the part, i.e., the larger the gain factor, the faster the heat will dissipate through the part by conduction. The procedure to calibrate the gain factor is reported in Section 3.2.1.

$$\mathbf{T}_c = \Phi e^{-\alpha g \Lambda t_b} \Phi' T_0 \quad (3)$$

Step 3(b): Heat loss through convection

Heat transfer by conduction between the nodes is followed in tandem with heat loss through forced and free convection from the nodes on the surface of the part. The temperature distribution after heat loss through forced and free convection, and through clamp conduction takes place for the duration of the time t_b , and is obtained as,

$$\mathbf{T}_b = \mathbf{T}_c e^{-\beta t_b}$$

$$\beta = \frac{h}{\rho \times L \times c_p} \quad (4)$$

Where h [$\text{W} \cdot \text{m}^{-2} \cdot \text{K}^{-1}$] is the heat transfer coefficient, ρ is the material density [$\text{kg} \cdot \text{m}^{-3}$], and L ($= 7.84$ mm) is the length of the block, and C_p is the specific heat [$\text{J} \cdot \text{kg}^{-1} \cdot ^\circ\text{C}^{-1}$] which is not a constant, but temperature-dependent in this work. The derived coefficient, β , is called the inverse time constant [s^{-1}]. The heat transfer coefficient h has two parts, to include both

free and forced convection. Heat loss due to forced convection is applied to the sides of the part and top of the substrate, as the carrier argon gas flows over these surfaces. Free convection is dominant on the sides and bottom of the substrate, where there is no active gas flow. The heat transfer coefficients are discussed in depth in Section 3.2.1.

In steps 3(a) and 3(b), for simplicity, we described the heating of only those blocks in the topmost layer. However, in DED the block immediately below the block being heated is also at an elevated temperature as the laser penetrates deeper. The heating of the blocks immediately below an actively heated block is implemented using Goldak's double ellipsoid model, and detailed in the forthcoming Section 3.3.

Step 3(c). Obtaining the temperature at the end of a layer after dwell

For each block-by-block iteration of step 3(a) and (b), the temperature of every node is recorded in a vector \mathbf{T}_b . This is repeated until an entire layer is simulated. After the process reaches the end of the layer, heat is allowed to dissipate by conduction immediately followed by convection in steps of 1 second, iteratively for a period equal to the dwell time (t_d). In this work, $t_d = 20$ s for Case A, and $t_d = 3$ s for Case B and Case C. In Eqns. (5) and (6) the time $t = 1$ s, and therefore the pair of equations are looped together for 20 times for Case A, and 3 times for Cases B and C to simulate the total dwell time between layers.

$$\mathbf{T}_{Lc} = \boldsymbol{\phi} e^{-\alpha g \Lambda t_d} \boldsymbol{\phi}' \mathbf{T}_b \quad (5)$$

$$\mathbf{T}_{Lf} = \mathbf{T}_{Lc} e^{-\beta t_d} \quad (6)$$

Step 4: Steps 3(a), (b), and (c) are looped until the last layer is built. The temperature of each node at each time step is recorded in a vector \mathbf{T} , which contains the thermal history of the part.

3.2.1 Implementation

The graph theory approach was implemented for predicting the temperature distribution of the three cases. Calibration was conducted at three different node densities. To arrive at these node densities, the thin wall and substrate were first randomly populated with nodes and then partitioned into discrete blocks, as depicted in Figure 8. A specified number of nodes were randomly allocated within each block (by the computer code). In this work, the effect of one, two, and three nodes within each block has been studied. Table 4 below provides further details about each of the three node densities.

Table 4. Three node densities, and corresponding simulation parameters ϵ and g .

Nodes per Block	Total Number of nodes	Node Density (nodes/mm ³)	Neighborhood Size, ϵ (mm)	Gain Factor (g)		
				$T_0 = 1900$ °C (mm ⁻²)	$T_0 = 2200$ °C (mm ⁻²)	$T_0 = 2450$ °C (mm ⁻²)
1	2830	0.2355	4.5	8	10	12
2	5660	0.4709	4.75	1	1.5	1.95
3	8490	0.7064	5.5	0.12	0.15	0.17

Case A was used for calibrating the parameters of the graph theory method – namely, the neighborhood size (ϵ) and gain factor (g) in Eqn. (3). Case A was chosen for calibration given the prominent temperature cycles therein as evidenced in Figure 4. The neighborhood size is defined as the radius of the imaginary sphere with a particular node at its center; it

determines the number of nodes connected to the node in the center of the sphere. Nodes within the volume of the sphere are connected to the node at its center while nodes outside the sphere are not connected to the central node. The gain factor (g) scales the rate of thermal diffusivity or heat flux between nodes. A higher gain factor increases the rate of thermal diffusion through the part (i.e., the larger the gain factor, the faster the heat will dissipate through the part).

An iterative grid search was performed to calibrate the gain factor and neighborhood size. The combination of neighborhood size and gain that resulted in the lowest mean absolute percentage error (MAPE) in Case A was selected and subsequently tested on Cases B and C. This calibration process was repeated for different node densities and melt pool temperatures. In other words, these simulation parameters had to be calibrated only once for a material and node density.

Three other heat transfer coefficients exist in the graph theory approach to the DED simulation; these were estimated in the calibration step and were held constant throughout all ensuing simulation cases, irrespective of node density or melt pool temperature. Table 5 includes the equivalent heat transfer coefficients for the three factors being discussed, along with the corresponding salient thermal phenomena number that describes them in Figure 3. The first of these factors is referred to as the clamp coefficient. As previously described in the experimental setup, the substrate was clamped at one end. From a heat transfer perspective, the surfaces of the substrate in contact with the clamp had an extra loss since the clamp acts as a heat sink. Therefore, this extra thermal pathway must be considered in the simulation. To account for the extra heat loss without simulating the

geometry of the clamp, an elevated loss was considered at the surfaces of the substrate in contact with the clamp. In other words, to approximate the large thermal conduction between the substrate and clamp in the experiment, a relatively large heat transfer coefficient was used on the appropriate surfaces.

Table 5. Equivalent heat transfer coefficients used in graph theory method.

Heat Transfer Coefficient	Inverse Time Constant in Graph-theoretic Method [s^{-1}]	Equivalent Heat Transfer Coefficient [$W \cdot m^{-2} \cdot K^{-1}$]	Corresponding Salient Thermal Phenomena Number
Clamp Coefficient	0.05	981.2	6
Forced Coefficient	0.0025	49.1	3, 4
Free Coefficient	0.00027	5.3	5

The process uses argon gas to propel titanium powder particles into the laser beam and melt pool. The argon gas continues down the sides of the thin wall while the deposition takes place. Although the sides of the thin wall and top surface of the substrate experience heat loss to a forced flow, the same cannot be assumed for the sides and bottom surface of the substrate. This necessitated a separate consideration of each boundary condition, thus necessitating the use of two distinct heat transfer coefficients. A forced heat loss coefficient was used to describe the forced convection loss caused by the argon shield gas flow originating from the four concentric nozzles. A free coefficient described the remaining free convection loss experienced at the sides and bottom surface of the substrate. These heat losses were divided into two separate components to account for the different flow regimes surrounding the part during the DED process.

Both factors were encapsulated under the broad term heat transfer coefficients, because, apart from conductive and convective heat transfer, heat loss also occurs through

radiation. An example calculation using the forced convection inverse time constant is included in Appendix A to demonstrate how equivalent heat transfer coefficients were found.

3.2.2 *Sensor Location*

A simulated sensor location identical to the location of the thermocouple from the experiment was necessary to validate the graph theory approach. In the graph theory approach, a cloud of nodes is used to approximate the part geometry as in step 1 of Figure 7, and the location of each node is identified by its Cartesian coordinates. A node closest to the sensor location was identified, and its Cartesian coordinates were modified to match those of the sensor location. Once it was moved to the thermocouple locations shown in Figure 6, the thermal history of the node was plotted against the experimental data reported by Heigel, et al. [7, 8]. This node is henceforth referred to as the *sensor node* in the context of the graph theory approach.

It is noted that the sensor node location was defined with a slight offset from the actual thermocouple location. This was to account for the fact that the thermocouples in the experiment were covered with aluminum tape to shield them from convection effects. Since the tape was not simulated in the graph-theoretic method, the sensor nodes were “buried” at a depth of 0.1 mm below the surface of the substrate. Since the graph-theoretic method applies convection losses only to exterior surfaces, the sensor node was essentially shielded by no longer being on the surface.

3.2.3 *Neighborhood size*

Neighborhood size, described in step 2 of Figure 7, was determined to be the proper method for this work. However, an alternative quantity that is referred to as “neighborhood number” was also explored. Whereas the neighborhood size defines a sphere of certain radius in which all nodes are connected to the central node, the neighborhood number defines the number of nodes to be connected to a central node, irrespective of spherical radius. For instance, a neighborhood number of ten will include the ten nodes closest to the central node. In a large body with a uniform node density, neighborhood size and number are one and the same, but it was determined that they become vastly different in certain cases.

Neighborhood number was first developed as a means to resolve a nonuniform node density in the graph-theoretic method. This nonuniformity was being explored because the substrate attached to each single-track thin wall was adding a relatively large computational load to the simulation. The obvious solution was then to populate the large substrate volume with fewer nodes since it was simply a large thermal mass acting as a heat sink for the high temperatures induced by the laser. By introducing a lower node density though, fewer substrate nodes fell into any central node’s neighborhood size. The result was a substrate that no longer removed heat from the thin wall since very few nodes were connected to the thin wall itself. With the lower nodal density, most substrate nodes were too far away to fall within the specified neighborhood size. Neighborhood number appeared to solve the problem by ensuring that regardless of distance from the central node,

a specified number of nodes would still be connected, thus reestablishing the numerous connections throughout the thin wall and substrate.

To fully investigate the neighborhood number and its effects, different location scenarios were introduced. It was quickly realized that sharp edges, and especially corners, became problematic for the neighborhood number. The problem is demonstrated in Figure 9, where neighborhood number enabled corner nodes to find just as many heat transfer “pathways” as a node in the center of the part. A corner node being able to transfer heat to the same number of neighbors as a central node is not consistent with reality, since the corner node is much more limited by the surface boundaries that surround it. This discovery prompted the author to use neighborhood size instead of neighborhood number to preserve the physics in the real system. Using neighborhood size also meant that a uniform density would have to be maintained throughout the part, including the substrate.

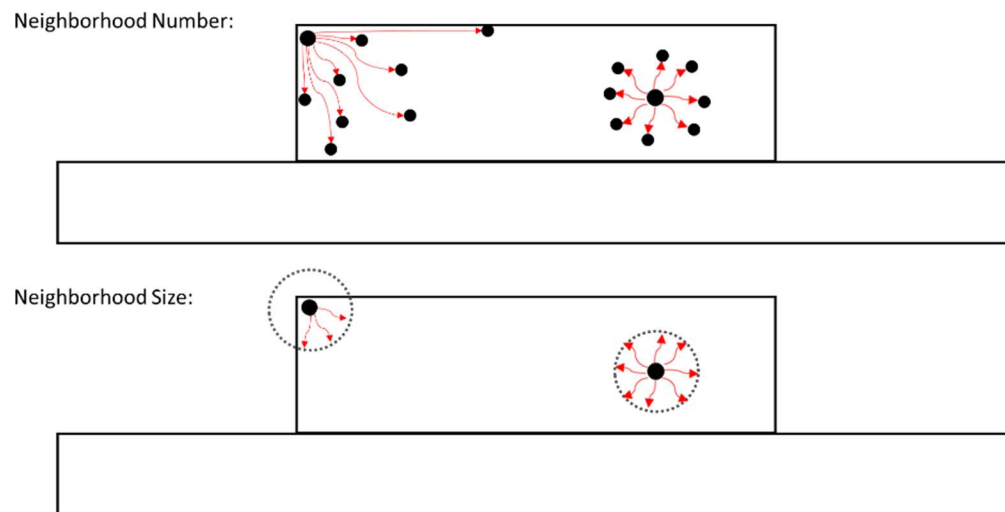


Figure 9. Heat transfer with neighborhood number vs. neighborhood size.

3.2.4 *Weight Scaling*

Another exploration that was conducted as part of this work involved weight scaling. To understand this concept, recall the network graph that was previously described as one of the major steps used by the graph-theoretic method. The nodes that fill the part are all linked together with an edge. Each edge has an associated weight that is based off of the Gaussian radial basis function, previously shown in Eqn. (1). It was the weight governed by the radial basis function that was being scaled before it went into the adjacency matrix.

Similar to the neighborhood number exploration described earlier, this scaling idea arose as a means to resolve the nonuniform node density between the wall and substrate. Due to the nonuniformity in density, the wall was much more efficient at transferring heat than the substrate. Instead of trying to resolve this discrepancy through an adjustment to the neighborhood parameter, like what was attempted and discussed earlier, it was believed that another possibility was to adjust the edge weights between certain nodes. By increasing the edge weights in the substrate, the nodes located therein would become better conductors of heat. This is because in the adjacency matrix, the respective edge weights have been adjusted so that the graph-theoretic method treats them as being closer to their partnering nodes than they are. Consequently, the node is able to accept more heat from its partner since it appears to be closer within the neighborhood. By doing this then, the conduction rates through the substrate can be made to duplicate those in the thin wall. This method of scaling the weights in the substrate was found to be effective and yielded promising results. However, the scaling factor that was found to resolve the nonuniformity was not able to be

thoroughly corroborated. Consequently, the method was abandoned due to its lack of rigor and substantial evidence.

3.2.5 Transient Material Properties

In all previous works, constant material properties have been assumed by utilizing an average thermal diffusivity term, α ($\text{m}^2 \cdot \text{s}^{-1}$). In contrast, the current work has defined thermal diffusivity as a function of temperature so that the graph-theoretic method can be further reconciled with reality. To accomplish this, the values in Table 6 were taken from Heigel, et al. and used to calculate corresponding thermal diffusivity values [7, 8]. For all calculated thermal diffusivity values presented in the table, a density of $4,430 \text{ kg} \cdot \text{m}^{-3}$ was used for Ti-6Al-4V [1]. After a temperature-dependent linear function, shown in Eqn. (7), had been fit to the calculated values, it was used to redefine the thermal diffusivity in the graph-theoretic method. This added capability allowed the graph-theoretic method to approximate a new thermal diffusivity value, α_{Layer} , for each layer based on the average temperature that occurred in the layer before it, T_{Layer} . Instead of fixing a thermal diffusivity value for the entire simulation, this updated approach requires only an initial value to be defined for the first layer.

Table 6. Temperature-dependent thermal properties for Ti-6Al-4V.

T [$^{\circ}\text{C}$]	k [$\text{W} \cdot \text{m}^{-1} \cdot ^{\circ}\text{C}^{-1}$]	C_p [$\text{J} \cdot \text{kg}^{-1} \cdot ^{\circ}\text{C}^{-1}$]	Calculated α [$\text{m}^2 \cdot \text{s}^{-1}$]
20	6.6	565	2.64
93	7.3	565	2.92
205	9.1	574	3.58
250	9.7	586	3.74
315	10.6	603	3.97
425	12.6	649	4.38
500	13.9	682	4.60

$$\alpha_{\text{Layer}} = 0.0042 \times T_{\text{Layer}} + 2.612 \quad (7)$$

3.3 Goldak's Double Ellipsoid Heat Source Model

Past works applying the graph theory approach to LPBF, assume that the laser elevates the nodes on the surface to the liquidous temperature [1-4]. In other words, in Eqn. (3), the nodes on the topmost layer have an initial temperature (T_0) which subsequently diffuses through the part. Typically, the temperature T_0 is set equal to the liquidus temperature of the material being deposited.

Setting the nodes on the topmost layer to the melting point implicitly assumes that the laser does not penetrate past one layer, and that the material at the bottom of that layer is solidified. However, this assumption in the context of the LPBF process does not carry over to DED, and therefore, needed to be relaxed. This is because, as noted previously, the laser velocity in LPBF is 10 to 30 times that of DED ($300 \text{ mm}\cdot\text{s}^{-1}$ versus $10 \text{ mm}\cdot\text{s}^{-1}$). At the same time, the laser beam has a diameter in the vicinity of $100 \mu\text{m}$, while the diameter of the laser beam in DED is closer to 1 millimeter. Consequently, the laser in DED penetrates deep, over multiple layers, into the part. Hence, in DED, not only are the nodes at the surface at an elevated temperature, but so also are nodes in prior layers, immediately below the laser path. Therefore, apart from considering only the surface nodes at a higher temperature, T_0 , it is necessary to initiate the sub-surface nodes with an elevated temperature.

To rigorously quantify the temperature reached by the sub-surface nodes, the heat source effects in DED were captured using the model created by Römer and Huis in 't

Veld [62, 63]. This model is encapsulated in a Matlab toolbox; the model shown in Eqn. (8) is a slightly revised version of Römer and Huis in 't Veld's equation.

$$T(x, y, z, t) = C \times P \times \frac{1}{2\pi K \sqrt{x^2 + y^2 + z^2}} \times \exp\left[-\frac{v}{2\kappa} \times \left(x + \sqrt{x^2 + y^2 + z^2}\right)\right] \quad (8)$$

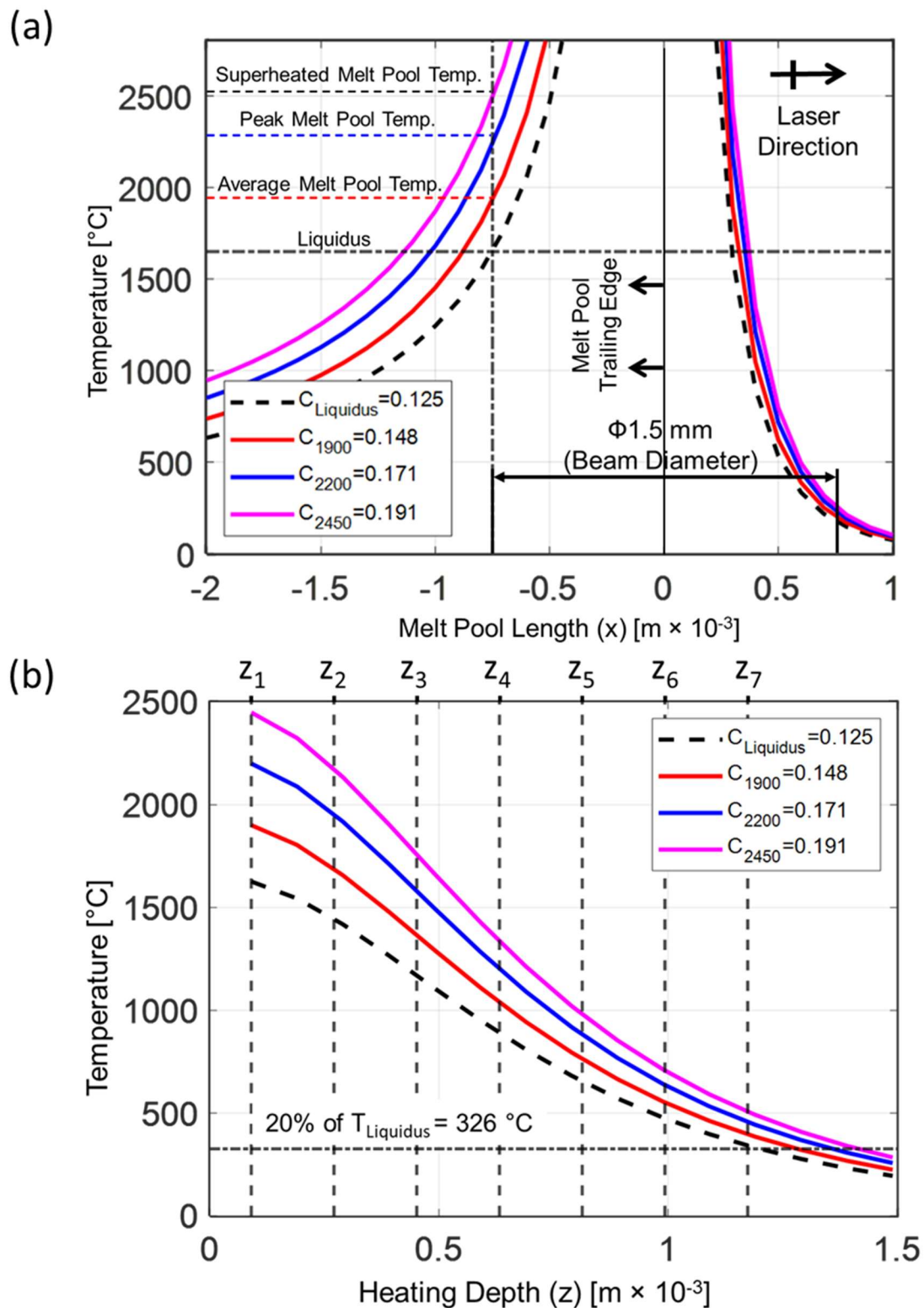
In Eqn. (8), The laser power, P, and scaling factor, C, are discussed in more detail in the following paragraph. The thermal conductivity is represented by K while the variables x, y, and z are local coordinates. The laser velocity and thermal diffusivity are represented by v and κ , respectively. Each variable is defined with appropriate units in Table 7.

Table 7. Variable definitions for Equation (8) [7, 8, 62, 63].

Variable	Units	Value
C	Dimensionless	0.125 to 0.191
Laser Power (P)	[W]	415
Laser Velocity (v)	[m·s ⁻¹]	8.5 × 10 ⁻³
Thermal Conductivity (K)	[W·m ⁻¹ K ⁻¹]	6.8
Thermal diffusivity (κ)	[m ² ·s ⁻¹]	2.7228 × 10 ⁻⁶

The equation was revised because the original one presented by Römer and Huis in 't Veld was found to have inconsistent units. To reconcile units, the laser power, P, and a unitless scaling factor, C, were included. The reason for the scaling factor becomes evident when considering how the model behaves around the origin, which corresponds to the center of the melt pool. Without the factor, the temperature profile approaches a vertical asymptote at the center of the melt pool. The scaling factor allows the user to essentially place an upper bound on the temperature profile. The upper bound coincides with the liquidus temperature of the material being deposited. In this work, the liquidus temperature was assumed to be 1630 °C for Ti-6Al-4V. Knowing that the laser diameter is 1.5 mm, it

was also assumed that the melt pool had an equivalent diameter to that of the laser heating it. Consequently, it was deduced that the liquidus temperature was reached at the periphery of the melt pool, which is depicted in Figure 11(a). This left the center of the melt pool to conceivably exceed the liquidus temperature by a considerable amount since it remained in the laser beam for a longer duration and was surrounded by molten Ti-6Al-4V. The other three scaling factors defined in Table 7 correspond to different assumed melt pool temperatures, which are discussed at the end of this section.



Recall that the purpose of the model is to predict the instantaneous temperature at any position relative to the center of the melt pool. This work leverages that prediction capability to understand the extent to which layers directly below the melt pool, referred to as sublayers, are heated. The temperature profile in Figure 10 has both a leading and trailing edge since the model assumes a heat source moving with constant velocity, v . It is intuitive then why the trailing edge in Figure 10 seems to decay slower than the leading edge. Whereas the trailing edge had already experienced the peak temperatures of the melt pool, the leading edge had yet to reach those levels as the laser and accompanying melt pool approached. Therefore, one must choose whether to apply the scaling factor C to the leading edge or trailing edge of the laser. Although a strong case can be made for either, the trailing edge was chosen in this work. The rationale behind that decision is discussed in the next paragraph.

Referring back to Figure 8, which demonstrates the graph-theoretic method's block-by-block heating scheme, it is evident that the laser heats each block over a discrete time period. Therefore, the laser in the model was not truly continuous. The specified time over which the laser heats a block was calculated based off block length and known velocity of the laser. The resulting heating duration for each block was found to be 0.92 seconds. Since the laser is quasi-stationary as it heats an individual block and those below it, it made the most sense to focus on the trailing edge when applying the scaling factor. After all, that edge corresponds to the portion that just experienced the laser beam's direct radiation. In the graph-theoretic method, the blocks have not *just experienced* the laser beam's radiation

but rather *are experiencing* it at that moment in time as the heat from the laser penetrates through multiple sublayers, as illustrated in Figure 11(b).

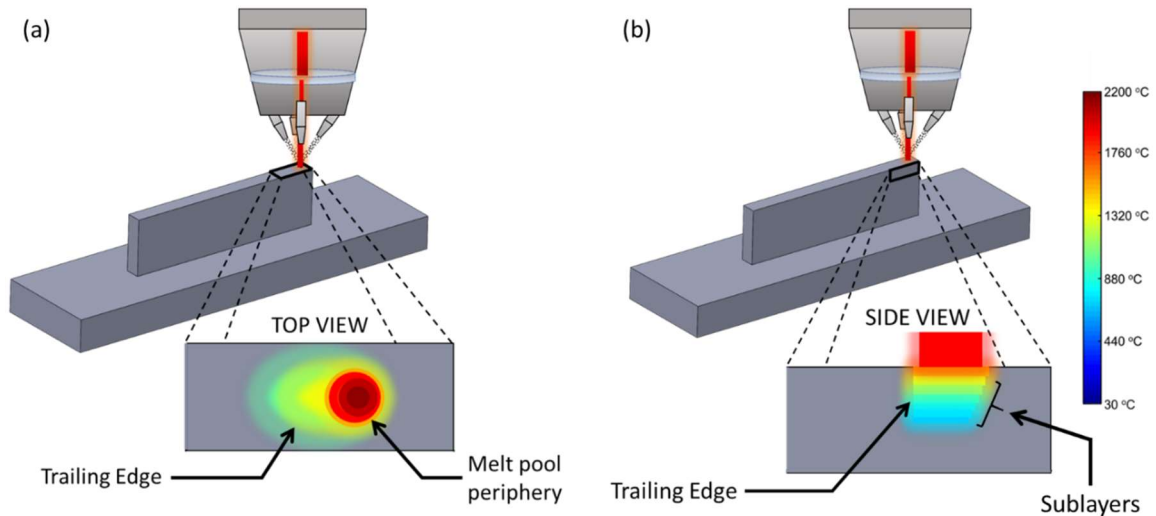


Figure 11. (a) Top View and (b) Side View of melt pool.

There are three major steps to obtaining the sublayer temperatures. These steps are described below.

1. Set a reference point from which all depths will be measured. The reference point in this work was set between the top layer, which receives the most direct radiation from the laser, and the first sublayer. This reference point was chosen because it was assumed that the molten Ti-6Al-4V reaches to at least the bottom of the first layer. If this were not true, it would be impossible for each deposited layer to be fused to the one under it. After the reference point has been set, determine relative depths for each sublayer. To best approximate the temperature in the sublayer blocks, depth measurements were taken at the middle, as opposed to the top or bottom, of each sublayer. Recall that the layer thickness in the experiment was

0.1806 mm. For this reason, the first sublayer temperature was taken at a depth of 0.0903 mm (half of the layer thickness).

2. Adjust the scaling factor C so that the temperature at the periphery of the 1.5-mm (dia.) melt pool matches the liquidus temperature (1630 °C). Save the resulting temperatures for each sublayer corresponding to the depths determined in step 1. Only sublayers with predicted values greater than 20% of the liquidus temperature were included in the graph-theoretic model, since those layers comprise most of the heat from laser penetration.
3. Input the saved temperatures into the model as values normalized to the liquidus temperature.

Critical to the model was the actual melt pool temperature which, as previously mentioned, would conceivably exceed the liquidus temperature. Given the wide range of melt pool temperatures used by other researchers and outlined in Table 2, three different temperatures were tested in a range of approximately 600 °C. The lowest of these was approximately 15% higher than the Ti-6Al-4V liquidus temperature at a value of 1900 °C. The other two melt pool temperatures considered were 2200 °C and 2450 °C. Together, these three temperatures represented an average melt pool temperature, peak melt pool temperature, and superheated melt pool temperature, respectively. Each temperature was simulated increasing the assumed temperature at the melt pool periphery by 15%, 35%, or 50%. The associated temperature profiles are presented in Figure 10. Ambient temperature of the argon gas in the chamber was assumed to remain at a constant 30 °C throughout each deposition.

4 Results

Figure 12 illustrates the simulation results at four different instances during the deposition process. These results were generated for the peak melt pool temperature (2200 °C). As expected, the highest temperatures were achieved in Case B, where no programmed dwell time was included. In contrast, Case A remained at the lowest temperature, which was due to the 20-second dwell time that was applied between each deposition layer. In the following sections, each case is considered individually, and their results are presented.

4.1 Case A Results

Figure 13 presents the simulation results and thermal history of the deposition using a 20-second dwell between layers (Case A). In the absence of melt pool temperature data from the experiment, three different melt pool temperatures were considered in the simulation. In addition, recall that three different node densities were also selected. Figure 13 shows the corresponding results for each melt pool temperature and node density. The calibration values that were determined from Case A (namely, neighborhood size and gain) are presented in Table 4. The neighborhood size is only dependent on node density. It is clear to see that an increased melt pool temperature resulted in larger temperature excursions during the deposition of each layer. This was especially noticeable at the higher node densities, where the prediction results seemed to be stretched vertically as one compared the lowest to highest melt pool temperatures. Due to the programmed 20-second dwell time, Case A resulted in the lowest peak temperature (200 °C) achieved between the three experimental cases.

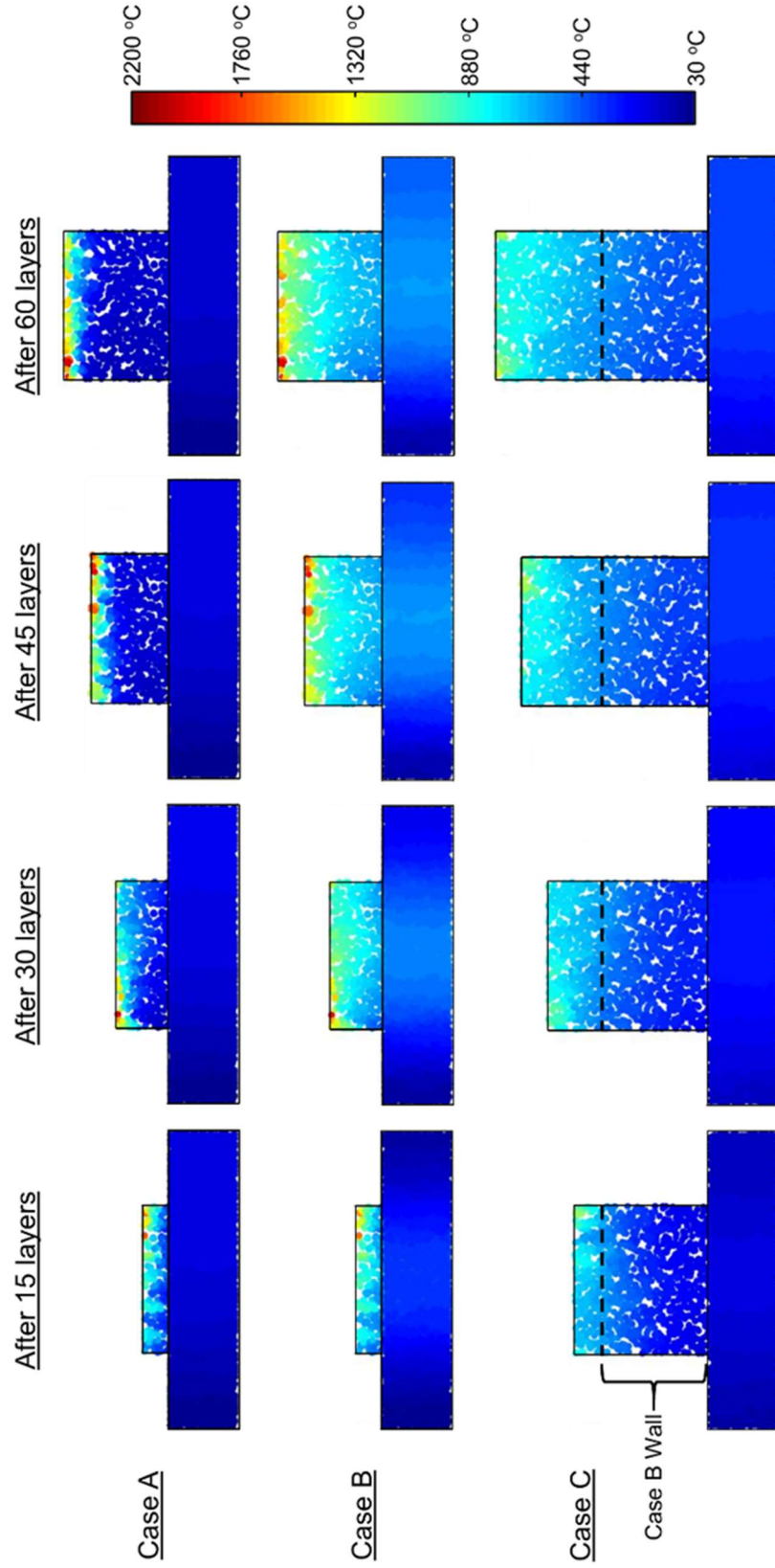


Figure 12. Snapshots of the graph theory-based simulation for each case. The lack of dwell time in Case B and Case C leads to accumulation of heat in the top layers of the part.

It may also be noted that the initial rise in temperature observed in the experiment is consistently higher than the graph theory predictions. The main reason for this early-time mismatch is that the gain factor was chosen based off of a calibration of the whole time domain. If the calibration step had only considered the first half of the experimental data, there would have been a smaller mismatch during that portion of the simulation. The portion of experimental data best suited for calibration of the graph-theoretic approach is dependent on the specific situation.

There are two other compounding assumptions in the simulation that could be further contributing to the early-time mismatch: (1) the constant ambient temperature consideration and (2) the laser only melts the material and does not impinge upon the substrate even for the first few layers. Regarding the first assumption, it is assumed that changes in ambient temperature over the course of the build are negligible. In turn, the ambient argon gas that surrounds the thin wall and substrate was fixed at a constant temperature of 30 °C. In reality, the envelope of argon that engulfs the part would experience a temperature increase as it reaches a new equilibrium, especially during the initial deposition layers. After transient heating of the gas during those initial layers, a constant ambient temperature assumption would again be more acceptable, but it would likely be higher than the initial temperature of 30 °C. If the elevated transient temperature of the gas were to be included in the model, it would lower its ability to remove heat from the thin wall and substrate, leading to a larger initial temperature rise in the prediction. Since the 30 °C temperature assumption was used in all simulation cases, this same explanation can be applied to all graph theory results. In the second assumption, the simulation assumes that the laser only melts the material and does not impinge upon the

substrate even for the first few layers. However, this is not the case, as in practice during the first few layers, the laser also strikes the substrate. This inherent laser impingement would tend to preheat the underlying material as new powder enters the laser beam and begins to stick to the substrate or previously deposited layers.

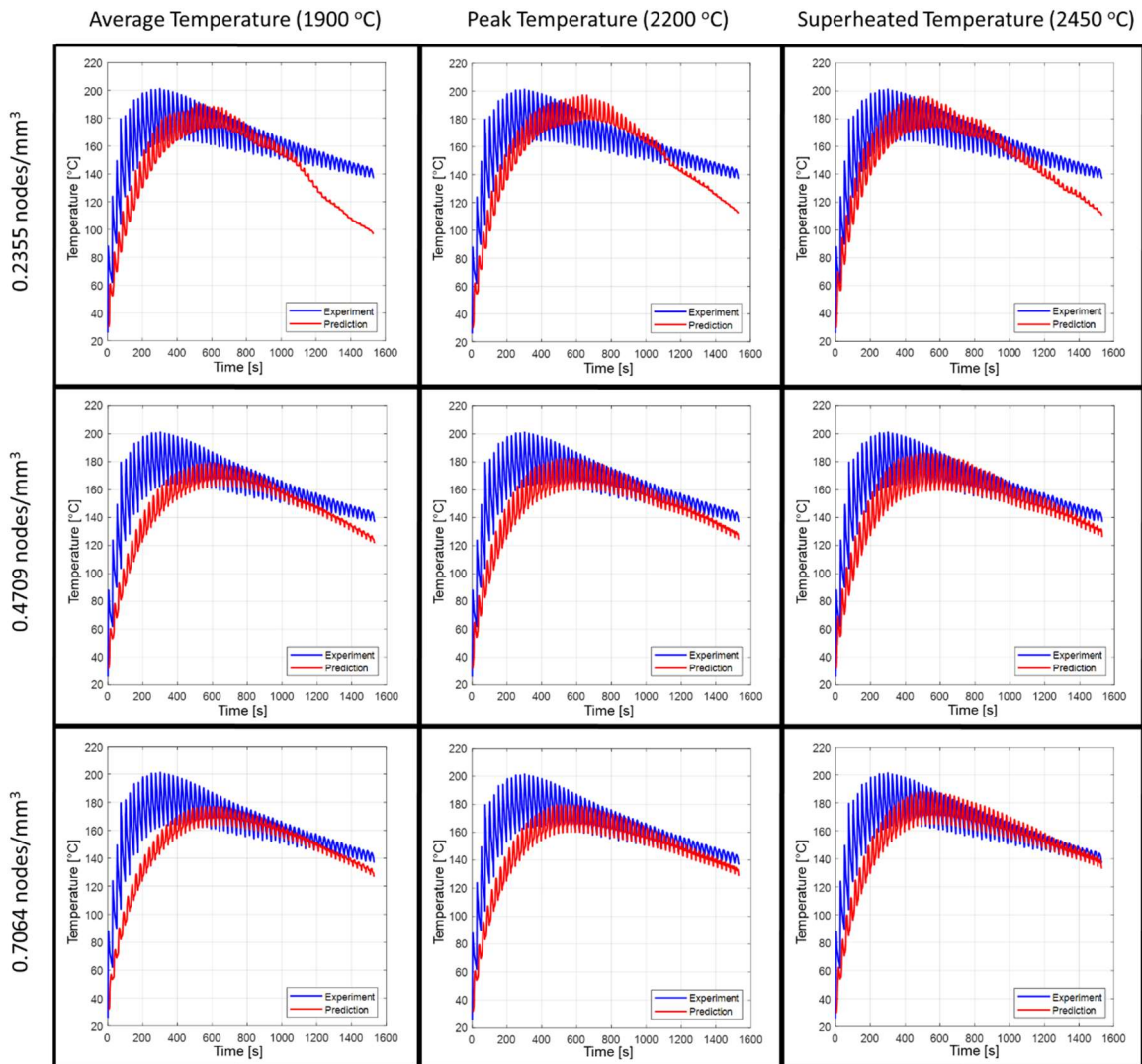


Figure 13. Simulation results for Case A.

Table 8 shows the corresponding errors and computation times for all Case A simulation results presented in Figure 13. The measured build time for Case A was approximately 26 minutes. Errors between the experimental thermal history and graph

theory simulation were calculated by comparing the measured temperature to the predicted temperature at instances in time. Two different methods of calculating errors were used in this work. Eqns. (9) and (10) show the mean absolute percentage error (MAPE) and root mean square error (RMSE), respectively:

$$MAPE = \frac{100\%}{n} \times \sum_{i=1}^n \left| \frac{T_i - \hat{T}_i}{T_i} \right| \quad (9)$$

$$RMSE = \sqrt{\sum_{i=1}^n \frac{(T_i - \hat{T}_i)^2}{n}} \quad (10)$$

where n is the number of instances in time that were compared over the duration of the deposition, i is the current instant of time, T_i is the measured temperature, and \hat{T}_i is the simulated temperature. The lowest MAPE was found to be approximately 6.0%.

Table 8. Summary table for Case A simulation.

Node Density [nodes·mm ⁻³]	Computation Time [min]	Data Points (n)	1900 °C		2200 °C		2500 °C	
			MAPE [%]	RMSE [°C]	MAPE [%]	RMSE [°C]	MAPE [%]	RMSE [°C]
0.2355	9	1800	13.10 (1.36)	25.92 (1.62)	10.75 (1.95)	23.21 (2.84)	10.13 (4.48)	21.48 (6.88)
0.4709	82		9.80 (0.61)	22.82 (0.99)	7.65 (1.28)	18.77 (2.05)	7.55 (2.34)	17.67 (3.75)
0.7064	194		7.95 (1.62)	20.70 (1.65)	6.60 (1.10)	18.39 (1.41)	5.98 (2.59)	16.54 (2.89)

4.2 Case B Results

Figure 14 presents the simulation results and thermal history of the deposition using a 3-second inherent dwell between layers (Case B). Corresponding results for each melt pool temperature and node density are shown. Due to the much lower dwell time, individual temperature excursions for each layer were much less pronounced. In addition, the lower

dwelt time resulted in a much higher peak temperature of nearly 500 °C in the experiment. The higher temperatures seen throughout the experiment also mean that the constant ambient temperature assumption described previously was less applicable in this case. Once again, it is suspected that this assumption led to a lower temperature rise in the simulation.

Also notable in this case, the graph theory simulation for the superheated melt pool temperature consistently ended with temperatures higher than those of the experiment. This was due to not enough heat being lost to the surroundings as it diffused downwards into the substrate, where the sensor is located. It is suspected that the apparent missing heat loss was likely a result of not directly considering radiation in the graph-theoretic model. As previously discussed, radiative heat loss is not explicitly included in the heat transfer coefficients applied to the part surfaces. However, it is recognized that a component of radiative heat transfer must exist in at least the forced coefficient, the one that is applied to the surfaces of the wall. As the deposition progresses upwards, higher temperatures will be observed in the newly deposited layers. This is because as the wall is built, it forms a longer “bottleneck” through which the heat must be conducted to reach the substrate. Consequently, the heat tends to congregate in the upper region of the thin wall. The growing region of elevated temperatures in the wall allows it to radiate more to the surrounding gas before it can diffuse downwards. This leads to the conclusion that a radiative heat loss term dependent on the wall height existed in the system. In contrast, the radiative heat loss that is currently assumed as part of the forced coefficient had a constant value, irrespective of wall height. A simple example of this phenomenon can be observed by watching a DED system build a thin wall. As the wall height increases, the uppermost

regions of the wall tend to glow brighter and longer, indicating that higher temperatures are being reached. This simple observation supports the idea that the heat tends to congregate in the upper portion of the wall. This congregation of heat results in higher radiative heat loss to the surroundings. Without a height-dependent radiative heat loss term in the graph-theoretic model, the elevated temperatures are left to diffuse downwards toward the sensor node, thus making the temperature prediction continue to climb. This hypothesis is supported by the graph theory simulations for Case A, where the much larger dwell time allowed the heat to diffuse downwards instead of congregate in the wall. This mitigated the variation in radiative heat loss over the course of the deposition and as a result, the graph theory simulation temperatures did not exceed those of the experiment at the end of the build.

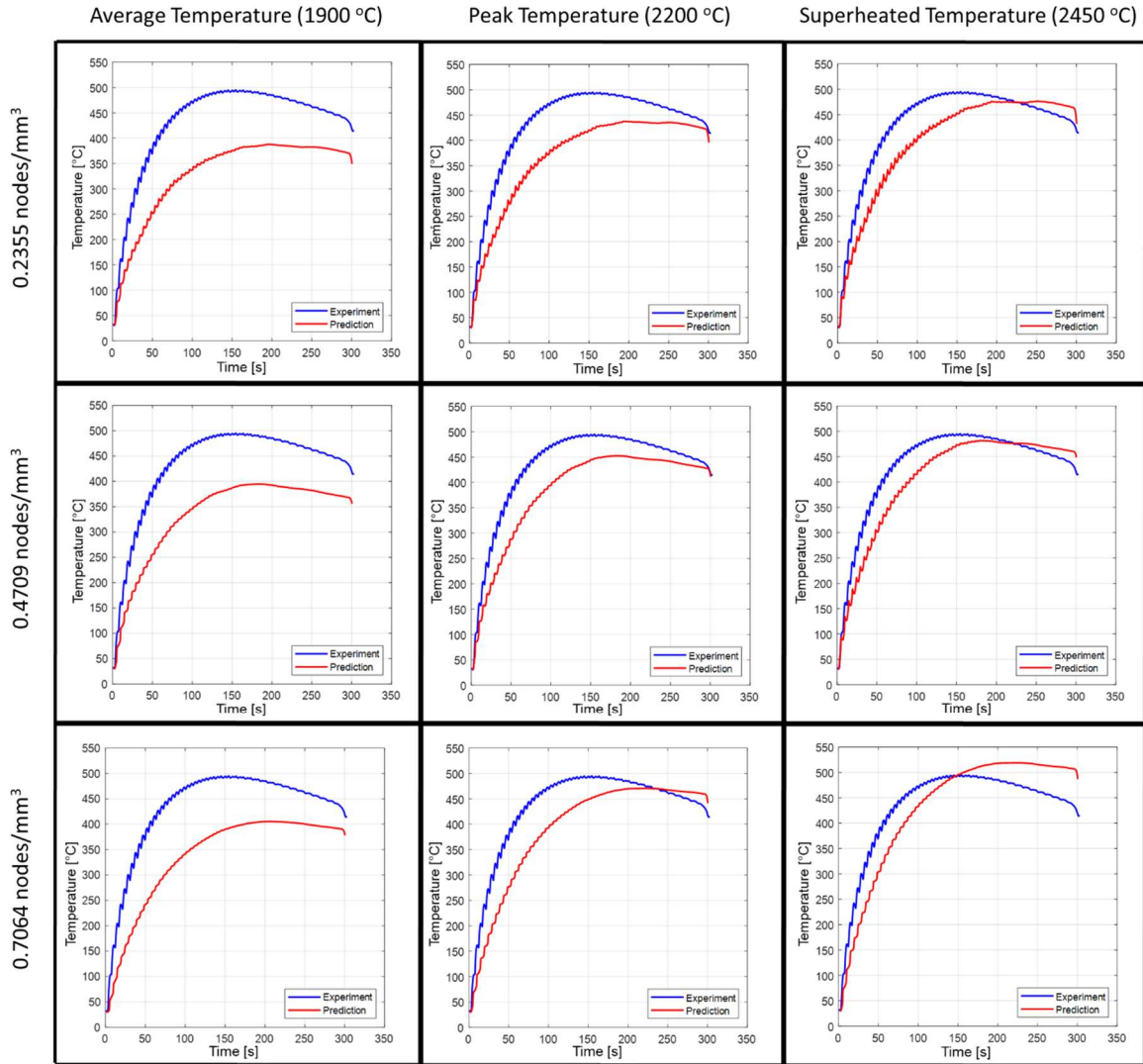


Figure 14. Simulation results for Case B.

Table 9 shows the corresponding errors and computation times for all Case B simulation results presented in Figure 14. The measured build time for Case B was approximately 5 minutes since the dwell time between layers was greatly reduced. Errors between the experimental thermal history and graph theory simulation were found to be larger than those for Case A. This is primarily due to Case A being the case used for calibration of the graph-theoretic model. The same calibrations found for Case A were directly applied to Case B to test the model. The lowest MAPE was found to be approximately 10.5%.

Table 9. Summary table for Case B simulation.

Node Density [nodes·mm ⁻³]	Computation Time [min]	Data Points (n)	1900 °C		2200 °C		2500 °C	
			MAPE [%]	RMSE [°C]	MAPE [%]	RMSE [°C]	MAPE [%]	RMSE [°C]
0.2355	9	900	26.54 (2.57)	114.37 (11.48)	17.33 (1.61)	75.04 (5.25)	10.49 (2.82)	48.46 (11.63)
0.4709	82		24.45 (1.89)	105.21 (8.23)	12.70 (0.54)	59.50 (2.42)	10.48 (0.90)	49.46 (3.58)
0.7064	194		22.56 (0.47)	97.95 (1.61)	12.48 (0.88)	57.80 (3.76)	12.38 (0.54)	53.28 (3.09)

4.3 Case C Results

Figure 15 presents the simulation results and thermal history of the deposition using a 3-second inherent dwell between layers for the double wall (Case C). Recall that this thin wall was built by first depositing the wall for Case B and after it had cooled, depositing another wall on top of it. Corresponding results for each melt pool temperature and node density are shown. As noted in Case B, individual temperature excursions for each layer were less pronounced due to the relatively short 3-second dwell time. Despite this wall being 124 layers tall instead of 62 layers, the lower dwell time still resulted in a peak temperature of nearly 300 °C, which is higher than that of Case A. It was observed that the graph theory simulation temperature tended to continue climbing past the experimental temperatures, especially when the melt pool temperature was assumed to be superheated. The same discussion regarding the height-dependent radiative heat loss term applies to this case.

It may also be noted that the rising action of the graph theory simulation was once again not as steep as that of the experiment. One explanation of this is related to the constant ambient temperature discussion, as previously described. Another explanation is related to

the geometry of the part. Since the Case C wall was twice as tall as the other walls and the lower half was deposited separately, the heat had twice as far to travel before it reached the sensor node. The previous calibration was not only determined for a wall that was half the height of the current one but also a wall that was at an elevated temperature for the entirety of the build. Since the walls in Cases A and B included layers that had only been deposited seconds or minutes before, they were hot to begin with. From Table 4, it is evident that thermal conductivity increases with temperature. It is suspected that the previously deposited wall composing the lower half of Case C, which was allowed to cool down before continuing, would have different material properties than that of the other walls. Additionally, it is known that the graph-theoretic model was calibrated for thin walls and substrate that were, in a sense, preheated since the deposition process was never stopped once it had started. In effect, the deposition process for Case C was equivalent to building on a new substrate that had both different thermal properties and a different geometry. It is suspected that these differences in properties and geometry compounded with the constant ambient temperature assumption to give the errors observed in Figure 15.

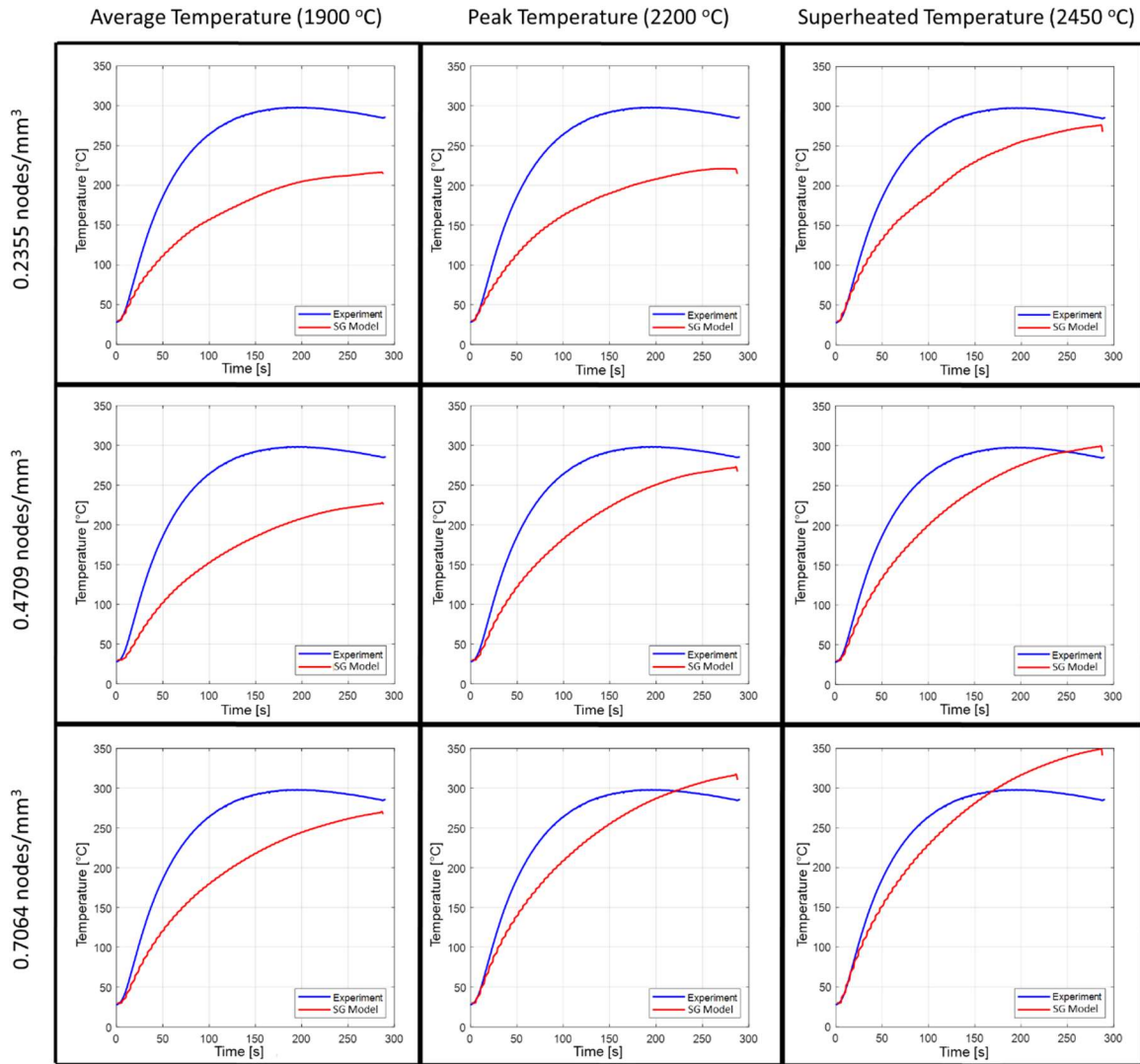


Figure 15. Simulation results for Case C.

Table 10 shows the corresponding errors and computation times for all Case C simulation results presented in Figure 15. The total build time for Case C was approximately 10 minutes since the dwell time between layers was once again only 3 seconds. Errors between the experimental thermal history and graph theory simulation tended to be the largest of any case, which is largely due to the compounding issues previously described. Case C was the second test case for the calibration values determined from Case A. The lowest MAPE was found to be approximately 9.5%.

Table 10. Summary table for Case C simulation.

Node Density [nodes·mm ⁻³]	Computation Time [min]	Data Points (n)	1900 °C		2200 °C		2500 °C	
			MAPE [%]	RMSE [°C]	MAPE [%]	RMSE [°C]	MAPE [%]	RMSE [°C]
0.2355	21	900	31.62 (3.98)	84.88 (10.69)	28.19 (2.02)	78.59 (5.51)	16.71 (0.49)	45.72 (1.57)
0.4709	188		31.96 (1.06)	84.02 (2.69)	19.72 (0.21)	51.74 (0.90)	12.51 (1.18)	35.03 (5.17)
0.7064	650		21.84 (1.12)	55.26 (3.35)	10.02 (0.69)	26.05 (3.26)	9.28 (3.40)	27.99 (14.63)

5 Conclusions and Future Work

Previous works have shown that spectral graph theory is a feasible method for relatively rapid simulation of the LPBF additive manufacturing process. The goal of this work was to test the graph-theoretic method on a different, and in many ways more challenging, additive process known as DED. For this to be accomplished, it was necessary to implement new considerations for the salient thermal phenomena that are unique to the process. It was found that by applying the graph-theoretic method to the thin wall deposition experiments, a calculated error of approximately 12% was attainable for each case (A, B, and C). Being the intermediate condition, the peak melt pool temperature case at 2200 °C was considered to be the best case to draw conclusions from. Meanwhile, the average melt pool temperature case attained a calculated error of 22% and the superheated melt pool temperature case typically achieved lower errors of approximately 10% or less for each case. Depending on how much accuracy one desires, an operator could run the simulation in as little as 9 minutes on a standard desktop computer.

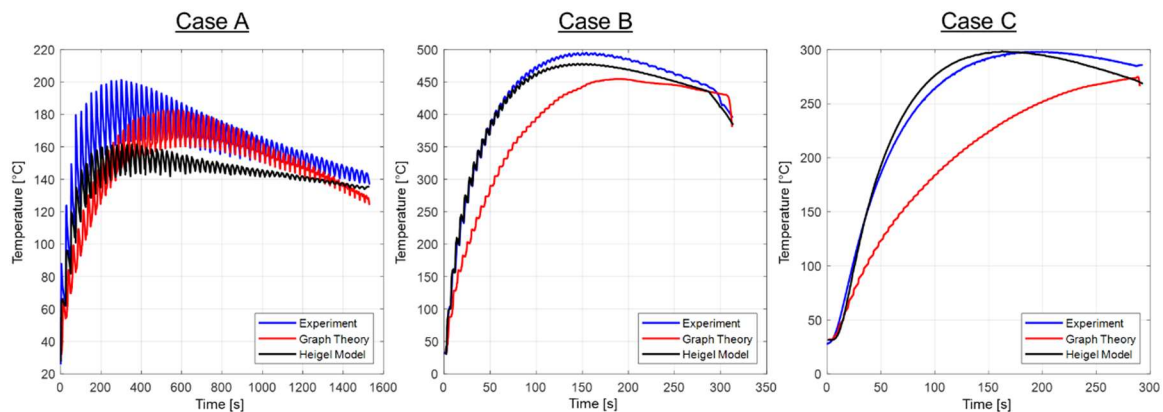


Figure 16. Case-wise comparison between the experiment, graph-theoretic model, and Heigel, et al. model.

Table 11. Prediction comparison between Heigel model and the graph-theoretic model for 2200 °C and 0.4709 nodes·mm⁻³.

Data	Case A		Case B		Case C	
	Time [min]	MAPE [%]	Time [min]	MAPE [%]	Time [min]	MAPE [%]
Heigel Model	136	10.4	136	2.4	No Report	4.1
Graph Theory	82	7.59	82	11.94	188	19.79
Build Time	25.6 minutes		5.2 minutes		10.1 minutes	

This work shows that the graph-theoretic method can provide valid thermal predictions for the DED process at a relatively low computational expense. A qualitative comparison between the graph-theoretic model, Jarred Heigel's model, and the experimental data is presented in Figure 16. The presented graph-theoretic results correspond with a maximum melt pool temperature of 2200 °C and a node density of 0.4709 nodes·mm⁻³. Table 11 provides a quantitative comparison between both models. It should be noted that the computation time reported for Heigel's model is for the part's half-symmetry. The graph theory computation time, on the other hand, is for the entire part. There are several improvements that can still be made to increase the prediction accuracy of the model. The following list outlines four main improvements for future work.

- **Obtain melt pool temperature directly from the experiment.** Due to inconsistencies in the melt pool temperatures measured by other researchers, three different temperatures were considered. As one can see from the results previously presented, the accuracy of the graph-theoretic method is directly dependent on the melt pool temperature. Therefore, narrowing down the temperature ranges seen at the melt pool level would allow for a better calibration and corresponding prediction.

- **Resolve disproportionate boundary node quantities.** With low node densities in narrow geometries like the one in the thin walls, current boundary node identification techniques begin to classify most of the nodes in the wall as boundary nodes. This is problematic because the extra heat losses associated with convection and radiation are applied to the boundary nodes. If nearly all of the nodes in the wall are being identified as part of the boundary, the entire wall effectively receives an additional heat loss that is only intended for the wall's exterior surfaces. This over application of heat loss can result in an unrealistically low temperature prediction. A subsequent investigation of the boundary node proportions used in this work was conducted and found that nearly 60% of the total number of nodes in the part were identified as boundary nodes for the lowest node density. In contrast, approximately 45% of the total nodes had been identified as existing on the boundaries for the higher node densities. It was then concluded that the lowest node density was experiencing 15% more in heat loss than its higher density counterparts. This disproportionality is most likely manifesting itself by increasing the overall errors.
- **Implement a more rigorous approximation for radiative heat loss.** As previously discussed, radiative heat loss effects are currently assumed to be accounted for as part of the forced coefficient. Considering how much radiative heat loss would vary across part geometries like the thin wall, a more rigorous approach to radiation may be necessary. Even if some radiative heat loss is currently being represented by the forced coefficient, it is evident that the loss

would not remain constant over time as the wall height increases with each new deposition layer.

A preliminary exploration into heat loss due to radiation was conducted for the three thin wall cases and is briefly discussed here. The steady-state radiation heat transfer equation is presented in Eqn. (11). In the equation, ε is the emissivity of the material (assumed to be 0.5 for Ti-6Al-4V), σ is the Stefan-Boltzmann constant, A is the surface area, T is the surface temperature, and T_∞ is the temperature of the surroundings. Since the graph-theoretic approach currently uses convective heat loss at the surface level to approximate other heat transfer mechanisms (i.e., conductive heat loss to the clamp and now radiative heat loss to the surroundings), an equivalent convective heat transfer coefficient must be found to represent radiation. Eqn. (12) shows the resulting equation, which is simply the steady-state convection equation with an added heat transfer coefficient, h_{rad} , to approximate heat lost by radiation. In that equation, h_c represents the heat transfer coefficient typically found in the convection equation. The result is an equation for total heat transfer at the surface, which is determined by adding the contributions of both heat transfer mechanisms. The next step was to define the h_{rad} term, which can be found in any heat transfer textbook. The final definition, taken from Cengel and Ghajar, is presented in Eqn. (13) [64].

$$q_{rad} = \varepsilon\sigma A(T^4 - T_\infty^4) \quad (11)$$

$$q = (h_c + h_{rad})A(T - T_\infty) \quad (12)$$

$$h_{rad} = \varepsilon\sigma(T - T_\infty)(T^2 + T_\infty^2) \quad (13)$$

The transient heat loss equation, defined in Appendix A, was then applied to determine the inverse time constant representative of the new radiative heat transfer coefficient, h_{rad} . After solving the transient equation for the inverse time constant representing radiation, the inverse time constant was added to its convective loss counterpart that was solved for in Appendix A. As previously stated though, the radiative heat loss term cannot be considered as a constant term, independent of time. As such, it is necessary to find a function that defines the inverse time constant for radiation as a function of temperature. To accomplish this, the average temperature of the top three deposition layers was determined. In other words, after every new layer had been deposited in the simulation, it would calculate the average temperature of the newly deposited layer along with the two layers below it to arrive at one average temperature. That average temperature is what determines the inverse time constant that governs radiative heat loss in the graph-theoretic model, thus giving an approximate radiative heat loss term that increases linearly with each new deposition layer.

The results of the exploration into radiation are presented in Figure 17. In the interest of time, only the lowest node density was considered with a melt pool temperature of 2200 °C. One should note that the added consideration of radiation appears to have had a significant impact on Cases B and C but little to no impact on Case A. This is due to the peak temperatures reached in each case. Since radiation is a temperature-dependent quantity and Case A achieved a lower peak temperature than the other two cases, a lower impact was observed. It is interesting, and not completely understood, why the added radiation appeared to significantly

improve the prediction for Case B but had an adverse effect on Case C. This may be related to the new part geometry present in Case C. More work needs to be done to investigate this phenomenon.

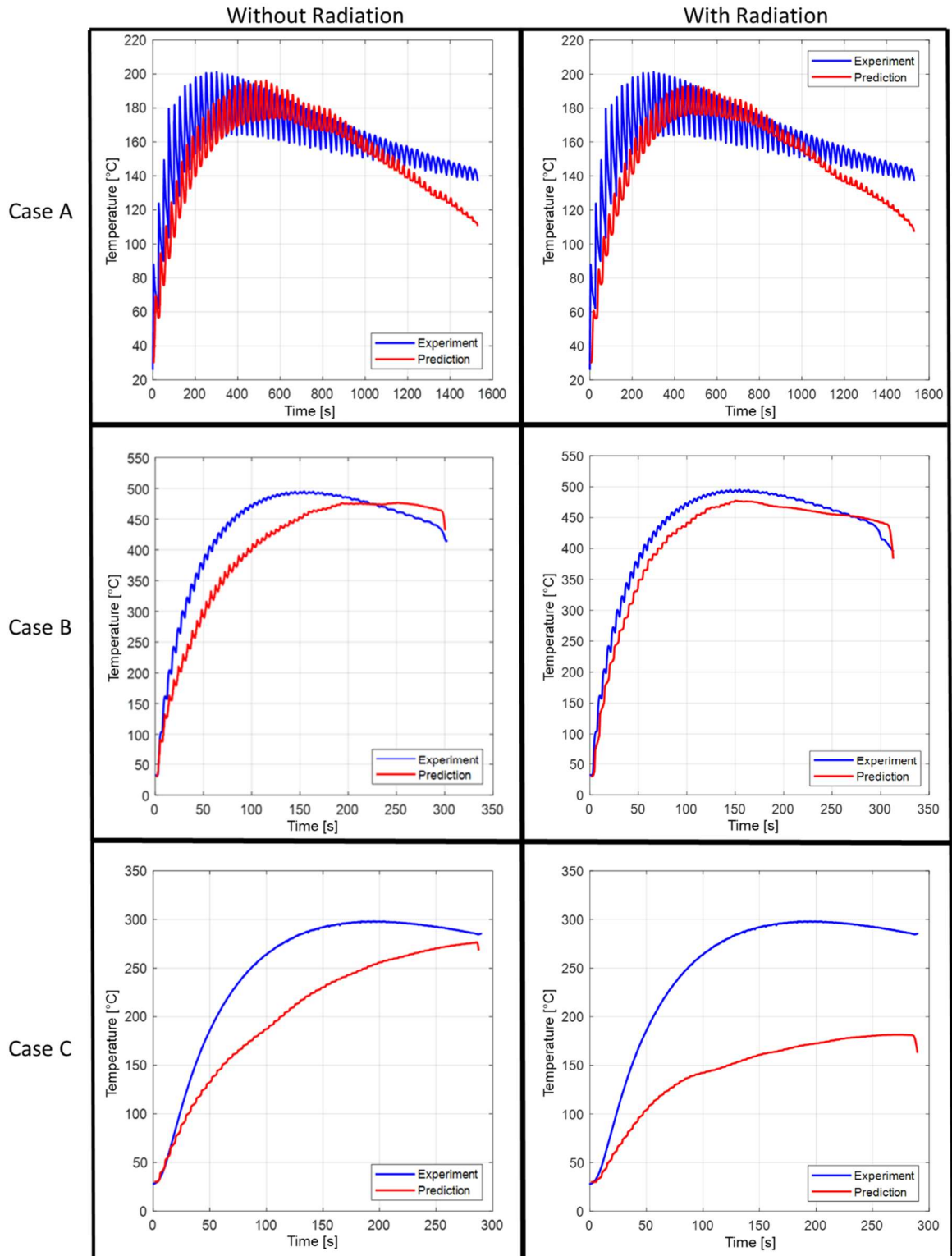


Figure 17. Case-wise radiation loss effects at melt pool temperature of 2200 °C and lowest node density.

- **Understand implications of the weight scaling method.** As previously described in Section 3.2.4, the method was found to be effective and yielded promising results. However, the factor used to scale the weights was not able to be entirely explained since the effects of weight scaling were not exhaustively investigated. Deeper exploration of the theory and application of this method would lead to a better understanding, which may allow it to be employed with more confidence. In turn, a model that can handle heterogeneous node densities would be extremely advantageous for investigating certain user-defined regions of the part. Areas of less interest could accordingly contain a lower number of nodes, thus reducing computation time. The weight scaling method could also lend itself useful to the simulation of a part containing multiple materials. The weights for each new material could be scaled in a way that is representative of each material's thermal properties, thus allowing the changing thermal gradients for different materials to be captured.

Appendix A. Heat Transfer Coefficient Calculation

$$\text{Transient Heat Loss: } \exp\left(-\frac{h \times A \times t}{\rho \times V \times c}\right) = e^{-\beta \times t}$$

$$\text{Solve for heat transfer coefficient: } h = \left(\frac{\beta \times \rho \times V \times c}{A}\right)$$

$$\text{Simplify: } h = (\beta \times \rho \times L \times c)$$

Variable	Value	Units
Heat Transfer Coefficient, h	49.1	$\text{W} \cdot \text{m}^{-2} \cdot \text{K}^{-1}$
Inverse Time Constant, β	0.0025	s^{-1}
Material Density, ρ	4430	$\text{kg} \cdot \text{m}^{-3}$
Block Length, L	0.00784	m
Specific Heat, c	565	$\text{J} \cdot \text{kg}^{-1} \cdot \text{K}^{-1}$

References Cited

- [1] M. R. Yavari, K. Cole, and P. Rao, "Thermal Modeling in Metal Additive Manufacturing using Graph Theory," *ASME Transactions, Journal of Manufacturing Science and Engineering*, vol. 141, pp. 071007-27, July 2019.
- [2] M. R. Yavari, K. D. Cole, and P. K. Rao, "Design Rules for Additive Manufacturing – Understanding the Fundamental Thermal Phenomena to Reduce Scrap," *Procedia Manufacturing*, vol. 33, pp. 375-382, 1/1/2019 2019.
- [3] K. D. Cole, M. R. Yavari, and P. K. Rao, "Computational heat transfer with spectral graph theory: Quantitative verification," *International Journal of Thermal Sciences*, vol. 153, p. 106383, July 2020 2020.
- [4] R. Yavari, J. Severson, A. Gaikwad, K. Cole, and P. Rao, "Predicting Part-Level Thermal History in Metal Additive Manufacturing Using Graph Theory: Experimental Validation With Directed Energy Deposition of Titanium Alloy Parts," in *ASME 2019 14th International Manufacturing Science and Engineering Conference*, 2019.
- [5] T. DebRoy, H. L. Wei, J. S. Zuback, T. Mukherjee, J. W. Elmer, J. O. Milewski, *et al.*, "Additive manufacturing of metallic components – Process, structure and properties," *Progress in Materials Science*, vol. 92, pp. 112-224, 3/1/2018 2018.
- [6] R. J. Williams, C. M. Davies, and P. A. Hooper, "A pragmatic part scale model for residual stress and distortion prediction in powder bed fusion," *Additive Manufacturing*, vol. 22, pp. 416-425, August 2018 2018.
- [7] J. C. Heigel, P. Michaleris, and E. W. Reutzel, "Thermo-mechanical model development and validation of directed energy deposition additive manufacturing of Ti–6Al–4V," *Additive Manufacturing*, vol. 5, pp. 9-19, 1/1/2015 2015.
- [8] J. C. Heigel, "Thermo-Mechanical Model Development and Experimental Validation for Directed Energy Deposition Additive Manufacturing Processes," Doctor of Philosophy Dissertation, Mechanical Engineering, Pennsylvania State University, State College, PA, 2015.
- [9] M. M. Francois, A. Sun, W. E. King, N. J. Henson, D. Tournet, C. A. Bronkhorst, *et al.*, "Modeling of additive manufacturing processes for metals: Challenges and opportunities," *Current Opinion in Solid State and Materials Science*, vol. 21, pp. 198-206, 8/1/2017 2017.
- [10] M. Labudovic, D. Hu, and R. Kovacevic, "A three dimensional model for direct laser metal powder deposition and rapid prototyping," *Journal of Materials Science*, vol. 38, pp. pages35–49, January 2003.
- [11] S. Zekovic, R. Dwivedi, and R. Kovacevic, "Thermo-structural finite element analysis of direct laser metal deposited thin-walled structures," *16th Solid Freeform Fabrication Symposium*, pp. 338-355, August 2005.
- [12] R. Jendrzewski, G. Śliwiński, M. Krawczuk, and W. Ostachowicz, "Temperature and stress fields induced during laser cladding," *Computers & Structures*, vol. 82, pp. 653-658, March 2004.
- [13] M. Chiumenti, M. Cervera, A. Salmi, C. A. d. Saracibar, N. Dialami, and K. Matsui, "Finite element modeling of multi-pass welding and shaped metal deposition processes," *Computer Methods in Applied Mechanics and Engineering*, vol. 199, pp. 2343-2359, 8/1/2010 2010.

- [14] A. Anca, V. D. Fachinotti, G. Escobar-Palafox, and A. Cardona, "Computational modelling of shaped metal deposition," *International Journal for Numerical Methods in Engineering*, vol. 85, pp. 84-106, 12/20/2010 2011.
- [15] S. Marimuthu, D. Clark, J. Allen, A. Kamara, P. Mativenga, L. Li, *et al.*, "Finite element modelling of substrate thermal distortion in direct laser additive manufacture of an aero-engine component," *Journal of Mechanical Engineering Science*, vol. 227, pp. 1987-1999, 12/21/2012 2013.
- [16] E. R. Denlinger, J. C. Heigel, and P. Michaleris, "Residual stress and distortion modeling of electron beam direct manufacturing Ti-6Al-4V," *Journal of Engineering Manufacture*, p. 11, 7/16/2014 2014.
- [17] L.-E. Lindgren, "Finite element modeling and simulation of welding part 1: Increased complexity," *Journal of Thermal Stresses*, vol. 24, pp. 141-192, February 2001.
- [18] L.-E. Lindgren, "Finite Element Modeling and Simulation of Welding part 2: Improved material modeling," *Journal of Thermal Stresses*, vol. 24, pp. 195-231, 7/29/2006 2001.
- [19] L.-E. Lindgren, "Finite element modeling and simulation of welding. Part 3: Efficiency and integration," *Journal of Thermal Stresses*, vol. 24, pp. 305-334, April 2001.
- [20] J. Goldak, A. Chakravarti, and M. Bibby, "A new finite element model for welding heat sources," *Metallurgical Transactions B*, vol. 15, pp. 299-305, June 01 1984.
- [21] V. Tikare, M. Griffith, E. Schlienger, and J. Smugeresky, "Simulation of coarsening during laser engineered Net-Shaping," Sandia National Labs, Albuquerque, NM (United States)1997.
- [22] W. Hofmeister, M. Wert, J. Smugeresky, J. A. Philliber, M. Griffith, and M. Ensz, "Investigation of Solidification in the Laser Engineered Net shaping (LENS) Process," *Journal of Metals*, vol. 51, 6/18/1999 1999.
- [23] A. J. Pinkerton and L. Li, "The development of temperature fields and powder flow during laser direct metal deposition wall growth," *Journal of Mechanical Engineering Science*, vol. 218, pp. 531-541, 5/1/2004 2004.
- [24] A. Vasinonta, J. L. Beuth, and M. Griffith, "Process Maps for Predicting Residual Stress and Melt Pool Size in the Laser-Based Fabrication of Thin-Walled Structures," *ASME Transactions, Journal of Manufacturing Science and Engineering*, vol. 129, pp. 101-109, 3/31/2006 2007.
- [25] L. Wang, S. D. Felicelli, and P. Pratt, "Residual stresses in LENS-deposited AISI 410 stainless steel plates," *Materials Science and Engineering A: Structural Materials*, vol. 496, pp. 234-241, 11/25/2008 2008.
- [26] S. M. Kelly and S. L. Kampe, "Microstructural evolution in laser-deposited multilayer Ti-6Al-4V builds: Part II. Thermal modeling," *Metallurgical and Materials Transactions A*, vol. 35, pp. 1869-1879, June 2004.
- [27] B. Zheng, Y. Zhou, J. E. Smugeresky, J. M. Schoenung, and E. J. Lavernia, "Thermal Behavior and Microstructural Evolution during Laser Deposition with Laser-Engineered Net Shaping: Part I. Numerical Calculations," *Metallurgical and Materials Transactions A*, vol. 39, pp. 2228-2236, 6/24/2008 2008.

- [28] R. Jendrzewski, I. Kreja, and G. Śliwińska, "Temperature distribution in laser-clad multi-layers," *Materials Science and Engineering A: Structural Materials*, vol. 379, pp. 313-320, 8/15/2004 2004.
- [29] P. Pratt, S. D. Felicelli, L. Wang, and C. R. Hubbard, "Residual Stress Measurement of Laser-Engineered Net Shaping AISI 410 Thin Plates Using Neutron Diffraction," *Metallurgical and Materials Transactions A*, vol. 39, pp. 3155–3163, 10/15/2008 2008.
- [30] X. He, G. Yu, and J. Mazumder, "Temperature and composition profile during double-track laser cladding of H13 tool steel," *Journal of Physics D: Applied Physics*, vol. 43, p. 015502, 12/7/2009 2010.
- [31] A. Lundbäck and L.-E. Lindgren, "Modelling of metal deposition," *Finite Elements in Analysis and Design*, vol. 47, pp. 1169-1177, October 2011.
- [32] A. F. A. Hoadley, M. Rappaz, and M. Zimmermann, "Heat-flow simulation of laser remelting with experimenting validation," *Metallurgical and Materials Transactions B: Process Metallurgy and Materials Processing Science*, vol. 22, pp. 101-109, February 1991.
- [33] K. Dai and L. Shaw, "Distortion minimization of laser-processed components through control of laser scanning patterns," *Rapid Prototyping Journal*, vol. 8, pp. 270-276, 12/1/2002 2002.
- [34] R. G. Cobonque, "Heat transfer between a flat plate and jets of airimpinging on it," in *International Conference on Heat Transfer, Part II*, 1962, pp. 454-460.
- [35] M. F. Gouge, J. C. Heigel, P. Michaleris, and T. A. Palmer, "Modeling forced convection in the thermal simulation of laser cladding processes," *The International Journal of Advanced Manufacturing Technology*, vol. 79, pp. 307–320, 2/4/2015 2015.
- [36] L.-E. Lindgren, "Numerical modelling of welding," *Computer Methods in Applied Mechanics and Engineering*, vol. 195, pp. 6710-6736, 10/1/2006 2006.
- [37] L.-E. Lindgren, *Computational Welding Mechanics: Thermomechanical and Microstructural Simulations*. Cambridge, England: Woodhead Publishing, 2007.
- [38] J. A. Goldak and M. Akhlaghi, *Computational Welding Mechanics*. New York, NY, USA: Springer, 2005.
- [39] *Minimization of Welding Distortion and Buckling: Modeling and Implementation*. Cambridge, England: Woodhead Publishing, 2011.
- [40] A. Bandyopadhyay and K. D. Traxel, "Invited Review Article: Metal-additive manufacturing—Modeling strategies for application-optimized designs," *Additive Manufacturing*, 2018.
- [41] E. R. Denlinger, M. Gouge, and P. Michaleris, *Thermo-Mechanical Modeling of Additive Manufacturing*: Butterworth-Heinemann, 2018.
- [42] P. Foteinopoulos, A. Papacharalampopoulos, and P. Stavropoulos, "On thermal modeling of Additive Manufacturing processes," *CIRP Journal of Manufacturing Science and Technology*, vol. 20, pp. 66-83, 2018/01/01/ 2018.
- [43] G. L. Knapp, T. Mukherjee, J. S. Zuback, H. L. Wei, T. A. Palmer, A. De, *et al.*, "Building blocks for a digital twin of additive manufacturing," *Acta Materialia*, vol. 135, pp. 390-399, 2017/08/15/ 2017.

- [44] W. J. Sames, F. List, S. Pannala, R. R. Dehoff, and S. S. Babu, "The metallurgy and processing science of metal additive manufacturing," *International Materials Reviews*, vol. 61, pp. 315-360, 2016.
- [45] B. Schoinochoritis, D. Chantzis, and K. Salonitis, "Simulation of metallic powder bed additive manufacturing processes with the finite element method: A critical review," *Proceedings of the Institution of Mechanical Engineers, Part B: Journal of Engineering Manufacture*, vol. 231, pp. 96-117, 2017/01/01 2015.
- [46] R. Jendrzejewski and G. Śliwiński, "Investigation of temperature and stress fields in laser clad coatings," *Applied Surface Science*, vol. 254, pp. 921-925, 12/15/2007 2007.
- [47] G. Zhu, A. Zhang, D. Li, Y. Tang, Z. Tong, and Q. Lu, "Numerical simulation of thermal behavior during laser direct metal deposition," *The International Journal of Advanced Manufacturing Technology*, vol. 55, pp. 945–954, 1/20/2011 2011.
- [48] S. Ghosh and J. Choi, "Modeling and Experimental Verification of Transient/Residual Stresses and Microstructure Formation in Multi-Layer Laser Aided DMD Process," *ASME Transactions, Journal of Heat Transfer*, vol. 128, pp. 662-679, 12/12/2005 2006.
- [49] R. Ye, J. E. Smugeresky, B. Zheng, Y. Zhou, and E. J. Lavernia, "Numerical modeling of the thermal behavior during the LENS® process," *Materials Science and Engineering A: Structural Materials*, vol. 428, pp. 47-53, 7/25/2006 2006.
- [50] P. Peyre, P. Aubry, R. Fabbro, R. Neveu, and A. Longuet, "Analytical and numerical modelling of the direct metal deposition laser process," *Journal of Physics D: Applied Physics*, vol. 41, p. 025403, 1/4/2008 2008.
- [51] P. Michaleris, "Modeling metal deposition in heat transfer analyses of additive manufacturing processes," *Finite Elements in Analysis and Design*, vol. 86, pp. 51-60, 4/28/2014 2014.
- [52] L.-E. Lindgren, H. Runnemalm, and M. O. Näsström, "Simulation of multipass welding of a thick plate," *International Journal for Numerical Methods in Engineering*, vol. 44, pp. 1301-1316, 3/30/1999 1999.
- [53] L.-E. Lindgren and E. Hedblom, "Modelling of addition of filler material in large deformation analysis of multipass welding," *Communications in Numerical Methods in Engineering*, vol. 17, pp. 647-657, September 2001.
- [54] Z. Yan, W. Liu, Z. Tang, X. Liu, N. Zhang, M. Li, *et al.*, "Review on thermal analysis in laser-based additive manufacturing," *Optics & Laser Technology*, vol. 106, pp. 427-441, 10/1/2018 2018.
- [55] M. Khanzadeh, S. Chowdhury, M. A. Tschopp, H. R. Doude, M. Marufuzzaman, and L. Bian, "In-situ monitoring of melt pool images for porosity prediction in directed energy deposition processes," *IISE Transactions*, vol. 51, pp. 437-455, 3/13/2018 2018.
- [56] G. J. Marshall, S. M. Thompson, and N. Shamsaei, "Data indicating temperature response of Ti–6Al–4V thin-walled structure during its additive manufacture via Laser Engineered Net Shaping," *Data in Brief*, vol. 7, pp. 697-703, June 2016.
- [57] Q. Yang, P. Zhang, L. Cheng, Z. Min, M. Chyu, and A. C. To, "Finite element modeling and validation of thermomechanical behavior of Ti-6Al-4V in directed energy deposition additive manufacturing," *Additive Manufacturing*, vol. 12, pp. 169–177, October 2016.

- [58] S. J. Wolff, S. Lin, E. J. Faierson, W. K. Liu, G. J. Wagner, and J. Cao, "A framework to link localized cooling and properties of directed energy deposition (DED)-processed Ti-6Al-4V," *Acta Materialia*, vol. 132, pp. 106-117, 6/15/2017 2017.
- [59] D. A. Kriczky, J. Irwin, E. W. Reutzel, P. Michaleris, A. R. Nassar, and J. Craig, "3D spatial reconstruction of thermal characteristics in directed energydeposition through optical thermal imaging," *Journal of Materials Processing Technology*, vol. 221, pp. 172-186, 2/21/2015 2015.
- [60] G. Marshall, W. J. Y. II, N. Shamsaei, J. Craig, T. Wakeman, and S. M. Thompson, "Dual Thermographic Monitoring of Ti-6Al-4V Cylinders during Direct Laser Deposition," in *International Solid Freeform Fabrication Symposium*, Austin, TX, USA, 2015, pp. 259-272.
- [61] F. R. K. Chung, *Spectral graph theory*: American Mathematical Society, 1997.
- [62] G. R. B. E. Römer, "Matlab Laser Toolbox User Manual," University of Twente, Enschede, Netherlands9/23/2010 2010.
- [63] G. R. B. E. Römer and A. J. H. i. t. Veld, "Matlab Laser Toolbox," *Physics Procedia*, vol. 5, pp. 413-419, 2010.
- [64] Y. A. Cengel and A. J. Ghajar, *Heat and Mass Transfer: Fundamentals & Applications*, 4 ed. New York, NY, USA: McGraw-Hill, 2011.